Supplementary information

Tracking intracellular forces and mechanical property changes in mouse one-cell embryo development

Marta Duch[1*], Núria Torras[1§*], Maki Asami[2*], Toru Suzuki[2*], María Isabel Arjona[1,3*], Rodrigo Gómez-Martínez[1], Matthew D. VerMilyea[4], Robert Castilla[5], José Antonio Plaza[1†] & Anthony C. F. Perry[2†]

Affiliations: [1]Instituto de Microelectrónica de Barcelona, IMB-CNM (CSIC), Esfera UAB, Campus UAB, 08193, Cerdanyola, Barcelona, Spain. [2]Laboratory of Mammalian Molecular Embryology, Department of Biology and Biochemistry, University of Bath, BA2 7AY, England. [3]Departamento de Electrónica y Tecnología de Computadores, Facultad de Ciencias, Universidad de Granada, 18071 Granada, Spain. [4]Ovation Fertility, 6500 N. Mopac Expy, Building #3 Suite #3102, Austin, Texas 78731, USA. [5]LABSON - Department of Fluid Mechanics, ESEIAAT-Universitat Politecnica de Catalunya, Terrassa.

[*]These authors contributed equivalently to this work.

[§]Current address: Biomimetic Systems for Cell Engineering, Institute for Bioengineering of Catalonia (IBEC), The Barcelona Institute of Science and Technology, Baldiri Reixac 10-12, 08028, Barcelona, Spain.

[†]Corresponding authors: joseantonio.plaza@imb-cnm.csic.es [J.A.P.] and perry135@aol.com [A.C.F.P.]

Supplementary Figures

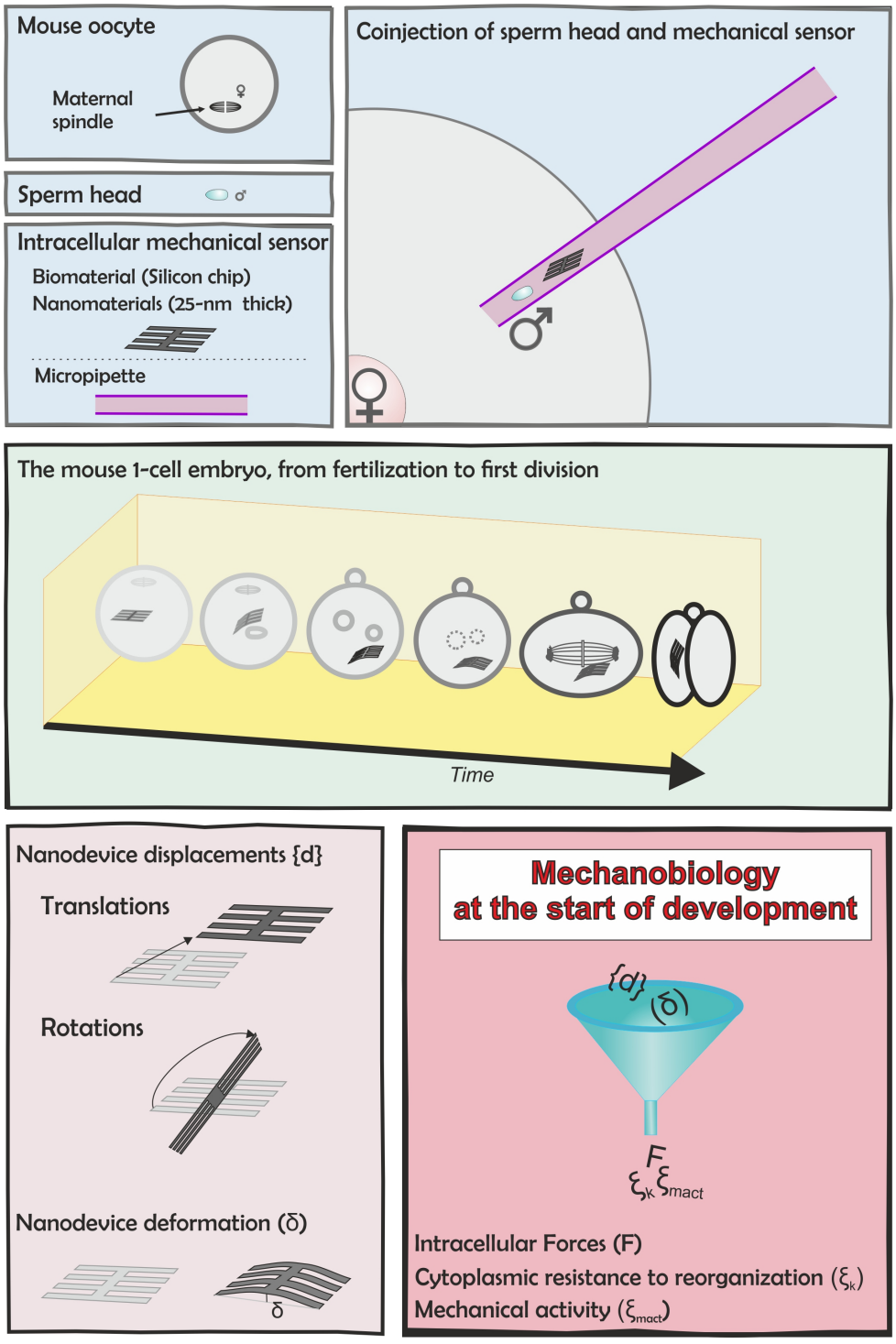

Supplementary Figure 1. Graphical abstract of the paper. Biology. Development of a one-cell mouse embryo from fertilization to the first cell division. Fertilization involves the combination (union) of an oocyte (egg) and a sperm. In many of our experiments, we achieve

fertilization by injecting a sperm head into an egg. **Biomaterials science and nanosystems.** We designed and fabricated silicon chip nanodevices that were 25 nm thick to act as mechanical sensors to address fundamental biological questions. Nanodevices were microinjected with a sperm head into a mouse oocyte, thereby initiating development. **Bioimaging**. Following sperm-nanodevice coinjection, we were able to monitor nanodevice displacement and bending in real-time movies as the embryos (containing nanodevices) developed. **Mechanobiology at the start of mouse development.** Analytical processing of nanodevice displacement and bending yields fundamental information about how forces and cytoplasmic properties contribute to initial developmental steps in mouse embryos.

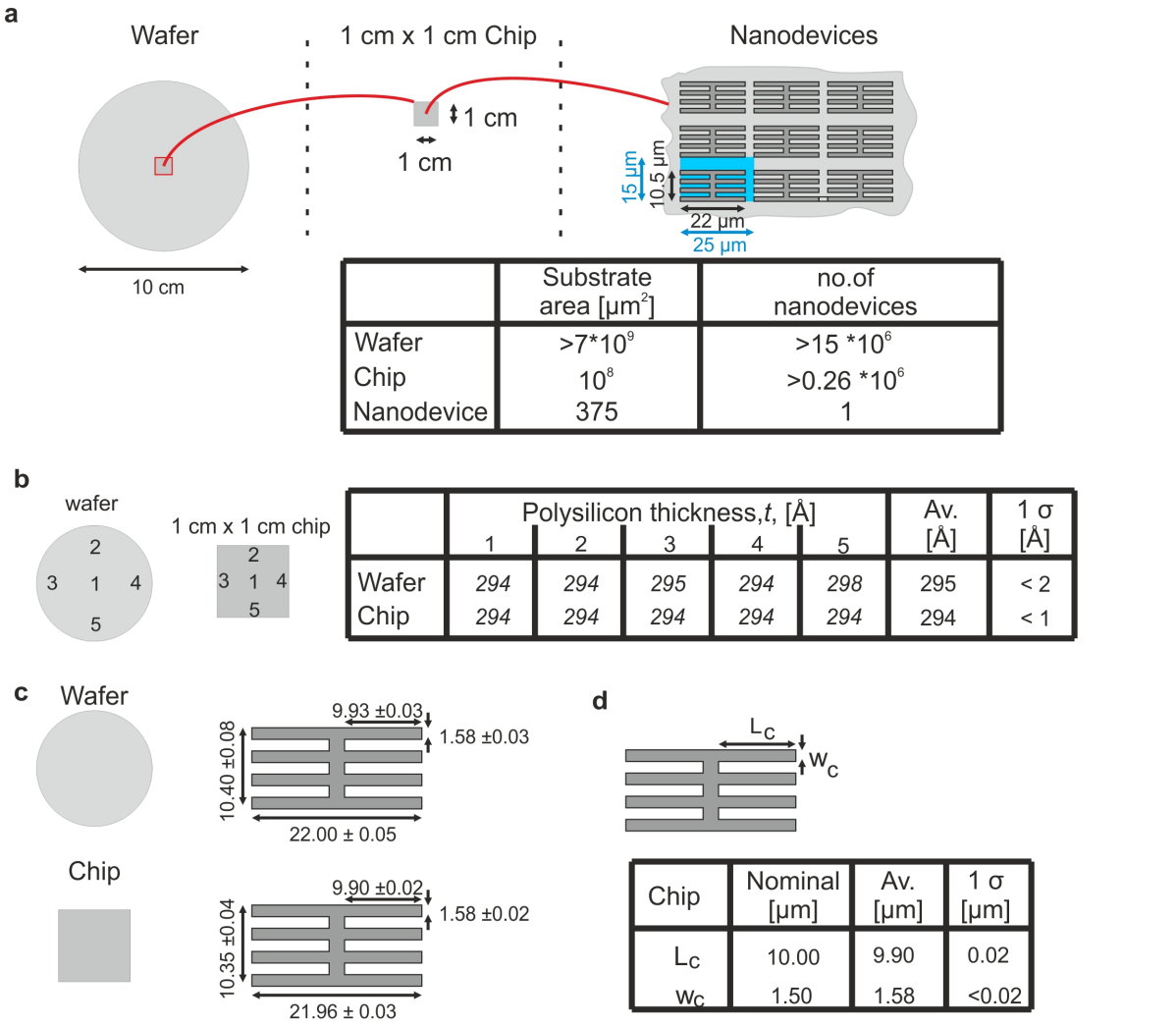

	Substrate area [µm²]	no.of nanodevices
Wafer	>7*10⁹	>15 *10⁶
Chip	10⁸	>0.26 *10⁶
Nanodevice	375	1

	Polysilicon thickness,*t*, [Å]					Av. [Å]	1 σ [Å]
	1	2	3	4	5		
Wafer	*294*	*294*	*295*	*294*	*298*	295	< 2
Chip	*294*	*294*	*294*	*294*	*294*	294	< 1

Chip	Nominal [µm]	Av. [µm]	1 σ [µm]
L_C	10.00	9.90	0.02
w_C	1.50	1.58	<0.02

Supplementary Figure 2. Reproducibility of nanodevice dimensions and the effects of geometrical and material property errors on device sensitivity. The use of standard techniques in microelectronics for the fabrication of the H-comb nanodevices allows

extraordinary control and reproducibility of geometrical dimensions during fabrication. **a**, Schematic (top) of the dimensions (left) of a silicon wafer, of the chip used for the experiments (center), and (right) showing the total area occupied by a nanodevice (area of the H-comb plus the area between nanodevices). The table below presents values for the area and number of fabricated devices per wafer and per chip. The technology allows the fabrication of >15 x 10^6 devices per wafer. Chips of 1 x 1 cm^2 containing >2.6 x 10^5 devices were used for the experiments in this work. **b**, A test wafer was processed to determine whether there was any variation in polysilicon thickness. Schematic (left) depicting the locations of five thickness measurements at wafer and chip levels. The polysilicon thickness was determined experimentally at these five points whose average values (± standard deviation, s.d.) are presented in the table (right). Polysilicon layers have been one of the materials most extensively used in microelectronics and MEMS such that polysilicon deposition techniques have been optimized over decades and offer consistently high thickness control and uniformity. As a standard procedure, the clean room routinely confirms high polysilicon thickness uniformity at five points around the wafer and the chip on a Nanometric Nanospec 2011. **c,** Average dimensions of the H-comb nanodevice and standard deviation for an entire wafer (top) and a chip at the center of the wafer. Standard photolithographic processes employed a Stepper NIKON Nsr 1505 G7e to allow a high degree of lateral control over H-comb device fabrication. **d**, Schematic (top) representing evaluation of lateral dimensional errors of the nanodevices. The table (lower) reports errors in dimensions L_c and W_c determined experimentally. **e**, Schematic (left) of cantilever loaded with a uniform pressure, *P*, and a cantilever loaded with a force, *F*, at one end. Analytical formula (center) describing the maximum bending of cantilever *versus P* and *F*; these give good approximations of the mechanics of H-comb devices for symmetric load conditions. Relative errors (right) are

shown that are due to the propagation of dimensional errors. Dimensional errors in the sensitivity of the nanodevices are very small and do not significantly affect the results. **f**, Relative error due to the propagation of errors in Young's modulus. **g**, Relative error due to the propagation of dimensional and Young's modulus errors. The main contribution to this error is from the calculation of Young's modulus.

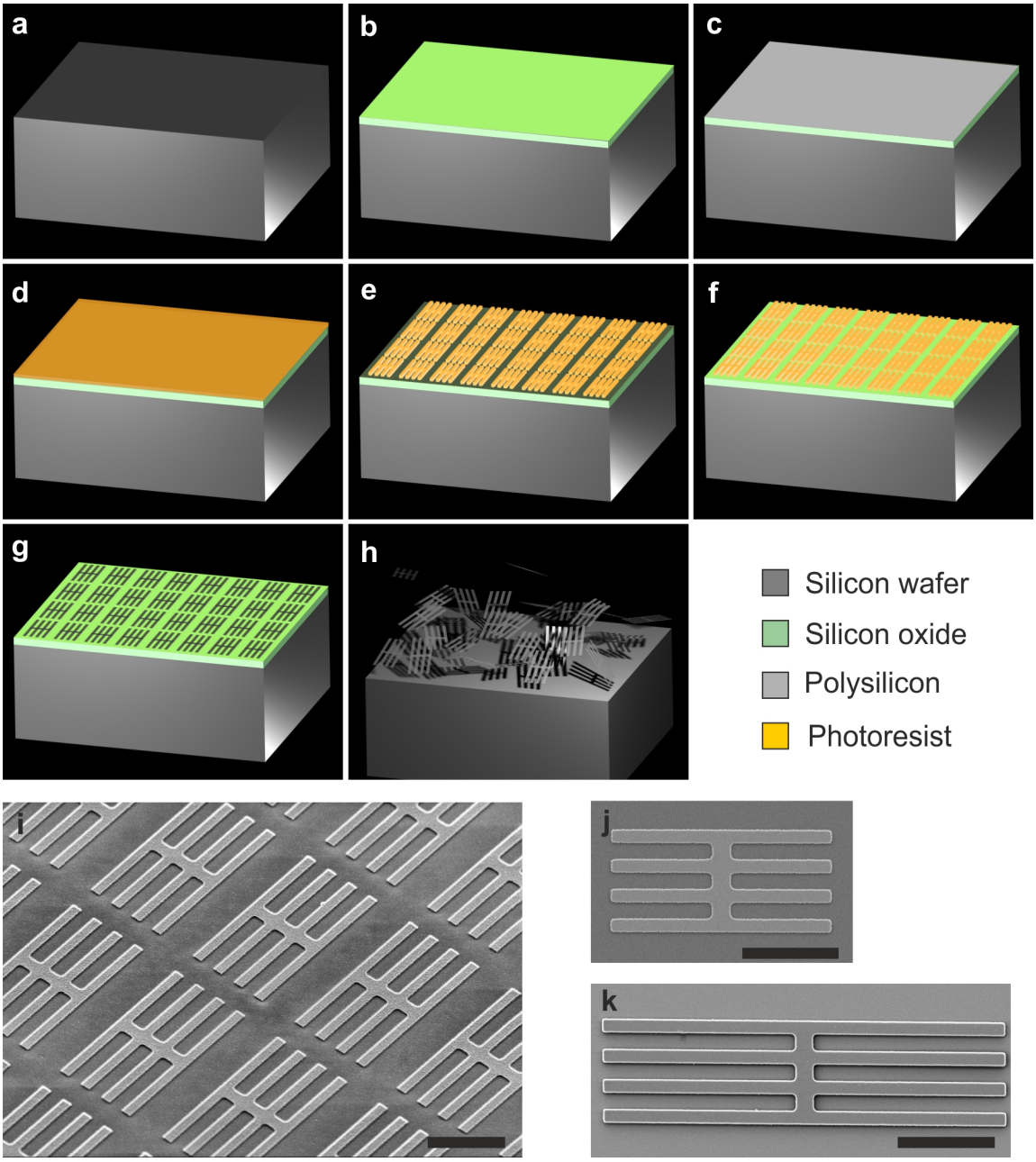

Supplementary Figure 3. Fabrication of H-comb nanodevices. Stages of device fabrication in sequence. **a,** Silicon wafer upon which the fabrication process begins. **b,** 100 nm SiO_2 (silicon oxide) sacrificial layer. **c,** A polysilicon layer (25-500 nm thick) is deposited as a structural material. **d,** A positive photoresist (1.2 μm thick) is spun onto the wafer. **e,** Photolithography defines the devices. **f,** Dry etching exposes the polysilicon. **g,** Photoresist stripping. **h,** Sacrificial etching by hydrofluoric acid (HF) vapour to release chips from the

wafer. **i**-**k**, Scanning electron microscope (SEM) images of fabricated devices at the wafer level, showing a group (**i**) and detail (**j**) of nanodevices of length 22 μm, with (**k**), a detail of a nanodevice of length 42 μm. Scale bar, 10 μm. Cantilevers and H-combs were fabricated using the same protocol.

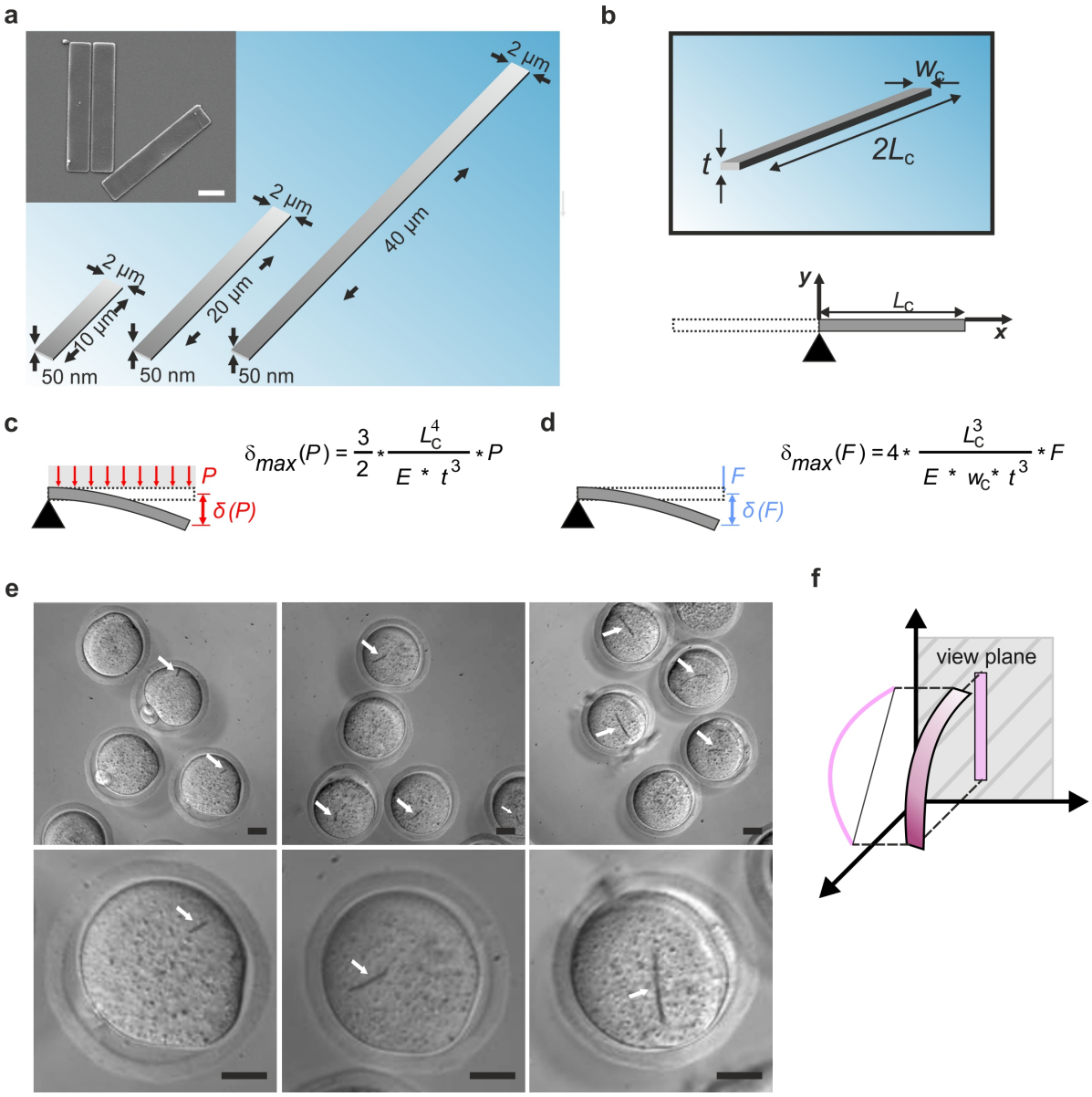

Supplementary Figure 4. Mechanical performance of cantilevers following microinjection into mouse oocytes. **a**, Schematic representation of fabricated cantilevers with different dimensions and (inset) SEM images of 10.0 x 2.0 x 0.05 µm cantilevers. Scale bar, 2 µm. **b**, Schematic of cantilever dimensions and a reduced model for mechanical analysis. Mechanical performance and formulas describing the maximum displacement, δ_{max}, *versus* (**c**) a uniform pressure applied to its upper surface, P, and (**d**) *versus* an applied force, F, at the end of the beam. Abbreviations are: Lc, length; wc, width; t, thickness; E, Young's

modulus for polysilicon. **e**, Hoffman modulation images of embryos respectively ~6 h after injection with a cantilever of dimensions 10.0 x 2.0 x 0.05 μm (left), 20.0 x 2.0 x 0.05 μm (center) and 40.0 x 2.0 x 0.05 μm (*n*=2 each), showing a corresponding oocyte at higher magnification in each case below. White arrows indicate the cantilever location inside embryos. Scale bar, 20 μm. **f**, Optical projection of cantilever of width 2.0 μm in the view plane can induce errors in the determination of its bending. *n* refers to independent experiments.

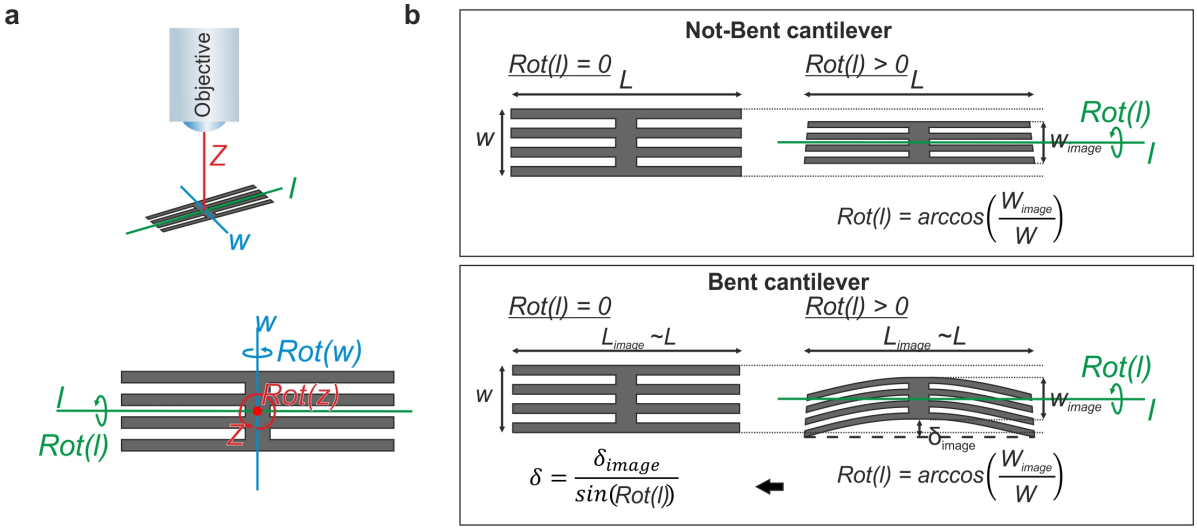

Supplementary Figure 5. H-comb nanodevice design. a, The eight-pronged H-comb nanodevice design avoids uncertainty in the determination of δ that arises for narrow devices that are not coplanar to the image plane (Supplementary Fig. 4e,f). Schematic representation shows the three axes of rotation. *Rot(z)* rotations do not affect the determination of δ (Supplementary Movie 1). *Rot(w)* rotations were not considered, as our experiments were restricted to analysis in which there was a reduced *Rot(w)*; larger *Rot(w)* produces images in which part of the device is out of focus and these images were excluded. **b**, Compared with single cantilever designs (Supplementary Fig. 4e,f), H-comb nanodevices allow the precise determination of *Rot(l)* rotation by determining the projected width of the device in the image, W_{image}, compared to the one of the design, W. The angle of rotation determined in this way was used to correct the empirical δ_{image}, to give δ.

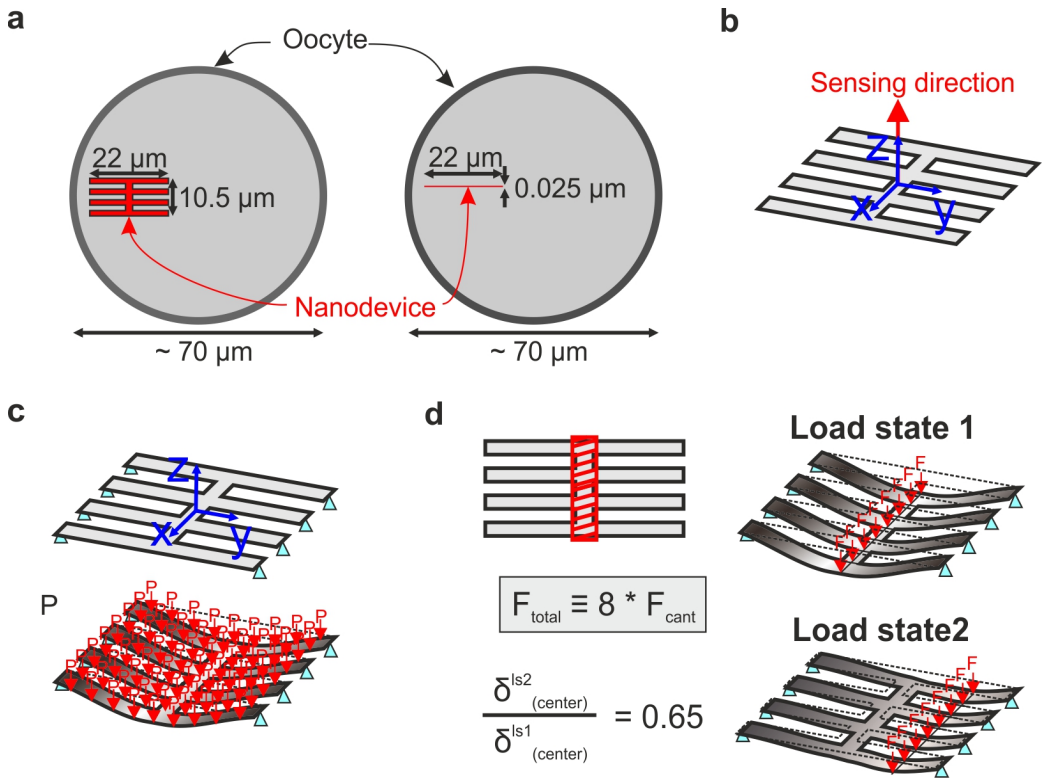

Supplementary Figure 6. The logic of H-comb design. **a**, In-plane dimensions (right) of H-comb devices (22 µm x 10.5 µm) were designed to be large enough to average random (local) molecular perturbations so that their intracellular behaviour would reflect mechanical load fluctuations and changes in cytoplasmic resistance due to cytoplasmic reorganization. Perpendicular dimensions were, by contrast, designed to be very small (0.025 µm) to allow a high sensitivity and to minimize the impact of devices on embryo development. **b**, The high-dimensional aspect ratio of H-comb nanodevices defines a sensing direction perpendicular to the plane of the device (nanodevice thickness, z-direction) to reduce cross-sensitivities (mechanical sensitivities to forces in the plane of the device, x and y directions). Moreover, 2D nanodevices possess an extraordinarily small volume; this is advantageous compared to 3D spherical beads or oil droplets which have much larger relative volumes that could perturb cytoplasmic dynamics. The H-comb devices used here have free spaces between the eight cantilevers, further minimizing any impact on cytoplasmic organization and molecular

diffusion compared with non-structured rectangular devices or spherical beads of similar micrometer-scale dimensions. The extraordinary aspect ratio of the nanodevices facilitates their responsive rotation inside the embryo, revealing cytoplasmic dynamics and mechanical activity. **c**, Since one purpose of the nanodevices is to detect the average of loads that drive cytoplasmic reorganization, as a first approximation we modelled bending based on P, applied to the device surface. Our boundary conditions assume that nanodevice ends are free to rotate and translate and that constraints in the perpendicular plane acting at the ends of the H-comb cantilevers are required to cause nanodevice bending. **d**, The logic of the devices (top left) maximizes the surface area at the center (14% of the total area) and the contribution (~25%) of loads applied to the center (red area) of the devices to effect bending. Considering this, and to improve comparison with other work in which the determined loads correspond to cellular forces, we modelled bending based on a total force, $F_{total} = 8 \times F_{cant}$, applied at the center of the device (top right). As an example, and to show that forces at the nanodevice center maximize bending, if the forces were applied closer to one border of the nanodevice (exactly mid-way along a cantilever), bending at the center would be -35% of the deformation induced by the same force acting at the center of the device. Thus, to achieve a given deflection by acting nearer to the nanodevice center, the force responsible would need to be larger; our force estimates therefore represent the low limit of the possible range of intracellular forces. Notably, the identification of different embryo phases by their characteristic force profiles, nanodevice rotations, effective stiffness and mechanical activity, corroborates the proposition that the main load contributions are at the center of the devices.

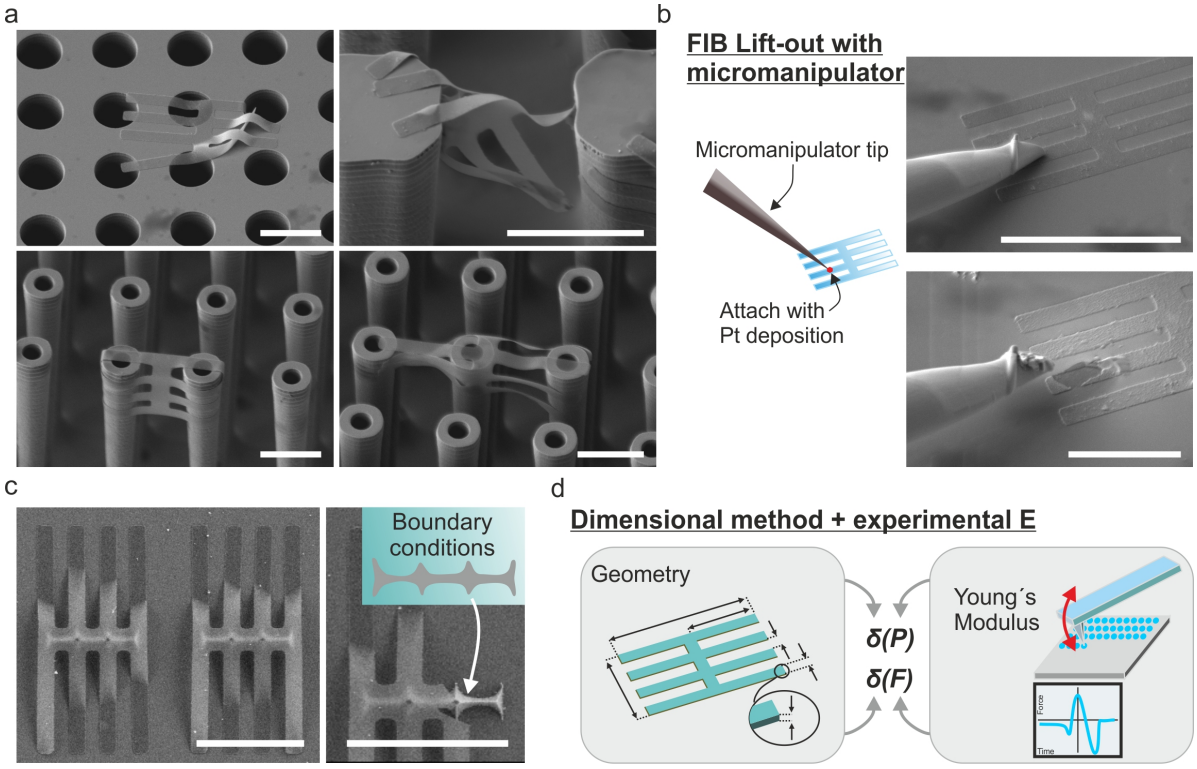

Supplementary Figure 7. Determination of H-comb nanodevice mechanical sensitivity. The stiffness of an arbitrary device depends on its geometry (shape and dimensions), the applied mechanical loads (*i.e.* Pressure, P, or Force, F…), and the applied boundary conditions (type and localization). Static and dynamic methods commonly used for the determination of the spring constant of simple microcantilevers and nanocantilevers (*i.e.* AFM probes) have important limitations for the determination of the mechanical sensitivity of H-comb nanodevices. These include reproducing the appropriate boundary conditions, reproducing applied load types and localization, and the difficulty of estimating sensitivity for non-simple geometric objects. In addition, the extremely low stiffness (elastic constant, $K < 10^{-3}$) of the nanodevices places non-trivial barriers on their manipulation after drying. Difficulties that prevent the use of static and dynamic methods are illustrated in **a-c.** **a**, Nanodevices immersed in ethanol and dropped onto a 3D microstructured substrate. The nanodevices are so soft that after drying they bend to adapt their shape to the 3D microstructures. **b**, A nanodevice laying

on a dry substrate is attached by platinum deposition to a micromanipulator tip in a SEM/FIB system. Nanodevices laying on a substrate stick so hard that when the micromanipulator lifts, they break rather than detaching from the substrate. **c**, Partial etching of the underlying sacrificial silicon oxide layer allows complete removal of the silicon oxide beneath the cantilever arms but not from the center of the H-comb devices. The attached zones are indicative of non-ideal boundary conditions. In addition the cantilevers stick to the substrate even though super-critical dry etching techniques were used. **d**, If the devices are simulated by numerical methods (*i.e* Finite Element Methods, FEM), dimensional models are not restricted to simple structures and simple boundary conditions and loads. Dimensional methods are commonly used in cantilever spring constant determination but are sometimes discarded in favour of static and dynamic methods due to errors in the geometrical measurement of the cantilevers[1]. Typical reported errors of ~16% were mainly due to uncertainties in the determination of the cantilever thickness (~5%)[1]. By contrast, the fabrication technology for the H-comb devices used here permitted a high degree of dimensional error control, so that they were <1.3% (Supplementary Fig. 2), rendering dimensional methods very attractive for accurate determination of their mechanical sensitivities.

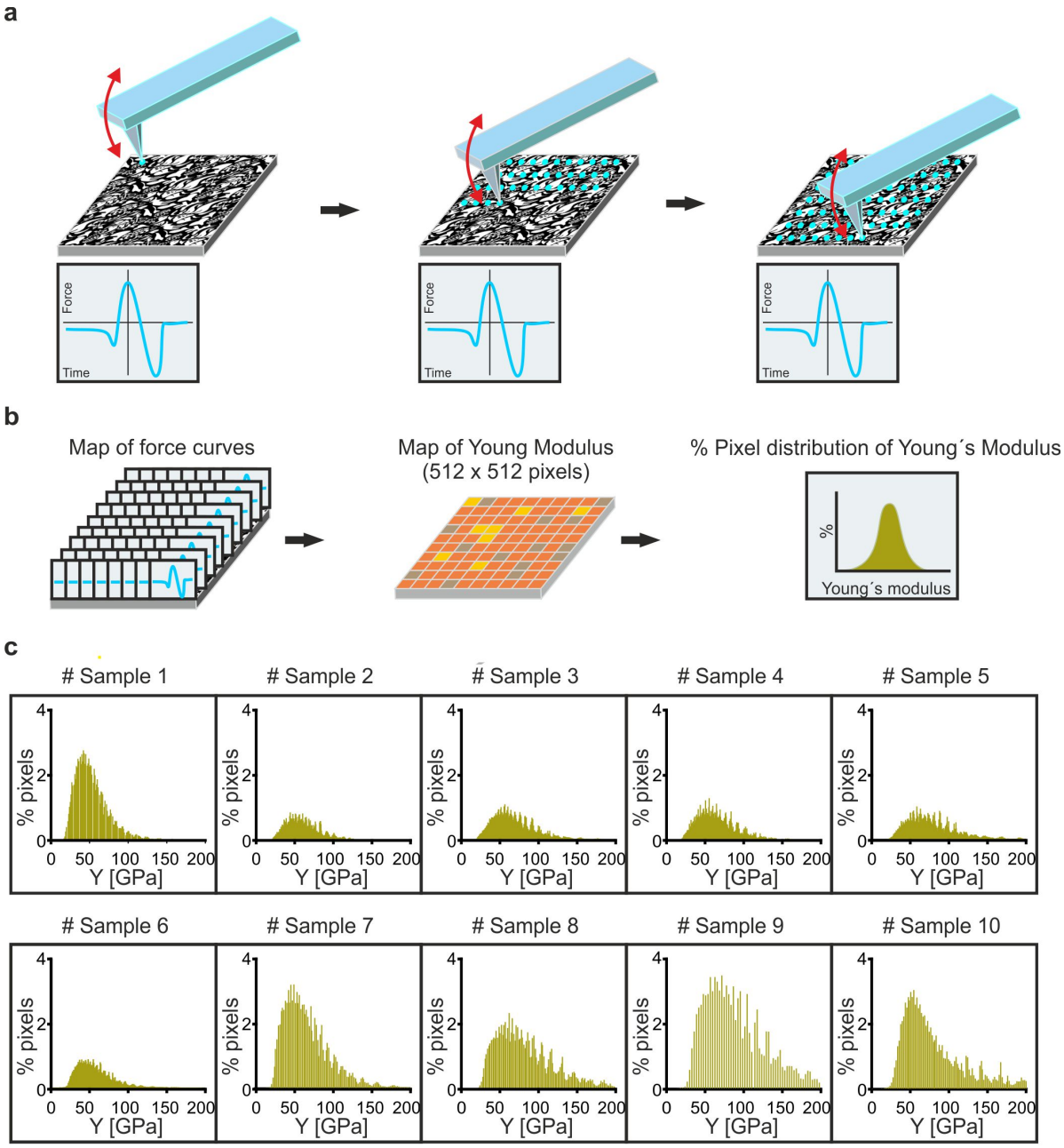

d

# Sample	1	2	3	4	5	6	7	8	9	10
Young´s Modulus [GPa]	43.711	51.767	55.066	53.169	59.974	50.560	46.960	63.936	66.527	52.247

Supplementary Figure 8. Experimental determination of Young's modulus for the 25 nm thick polysilicon layer using the Peakforce QNM method. **a**, Special imaging mode for atomic force microscopy where (**b**) the probe acquires a map of force-curves obtaining multiple mechanical properties, including a map of the Young's modulus of the nanolayer. **c**,

Experimental values of the percentage of pixels with the same Young's modulus measured in 10 samples of polysilicon layers 25 nm thick. **d**, Characteristic Young's modulus (the maximum of the Gaussian-like adjusted curve) for the 10 samples. Their average was adopted as the experimental Young's modulus for the H-comb devices.

5

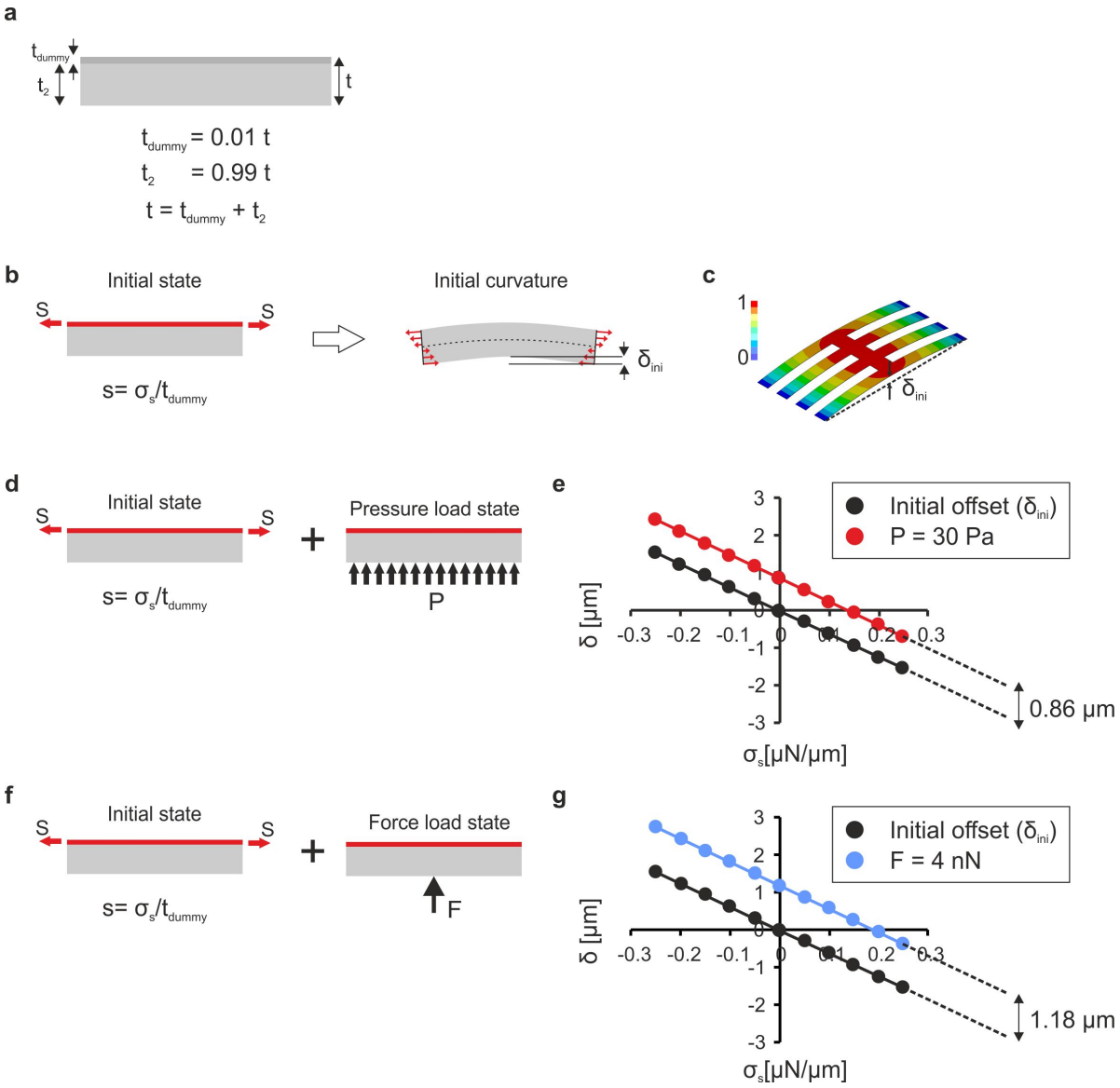

Supplementary Figure 9. Initial curvature of the nanodevices. Nanodevices show initial curvatures in the range of 1.3±0.3 µm due to intrinsic stress gradients, which induce a small initial deflection (δ_{ini}). **a,** Schematic of a lateral view of the model used to simulate initial nanodevice deflection due to an intrinsic stress gradient. The structure is simulated by considering two layers, the sum of whose thicknesses is the total thickness of the devices. **b**, The upper layer (left) is used as a dummy layer to apply a stress load (right) that induces a stress gradient and bends the devices. **c**, Normalized vertical displacement of a nanodevice due to intrinsic surface stress. **d**, Schematic of a model assuming an initial intrinsic curvature

and pressure load state, P. **e**, Simulated displacement (δ) *versus* a representative surface stress for the case of (**d**), with a representative P = 30 Pa. Displacement (δ) curves, considering either the surface stress alone, or the surface stress plus pressure, are parallel. This shows that the initial curvature of the nanodevice does not affect its mechanical sensitivity. **f**, Schematic of the model assuming an initial intrinsic curvature and force load state, F. **g**, Simulated displacement (δ) *versus* the surface stress for the case of (**f**), with a representative F = 4 nN. Displacement (δ) curves, considering either the surface stress alone, or the surface stress plus force, are parallel. These (**e, g**) further demonstrate that the initial curvature of the nanodevice does not affect its mechanical sensitivity.

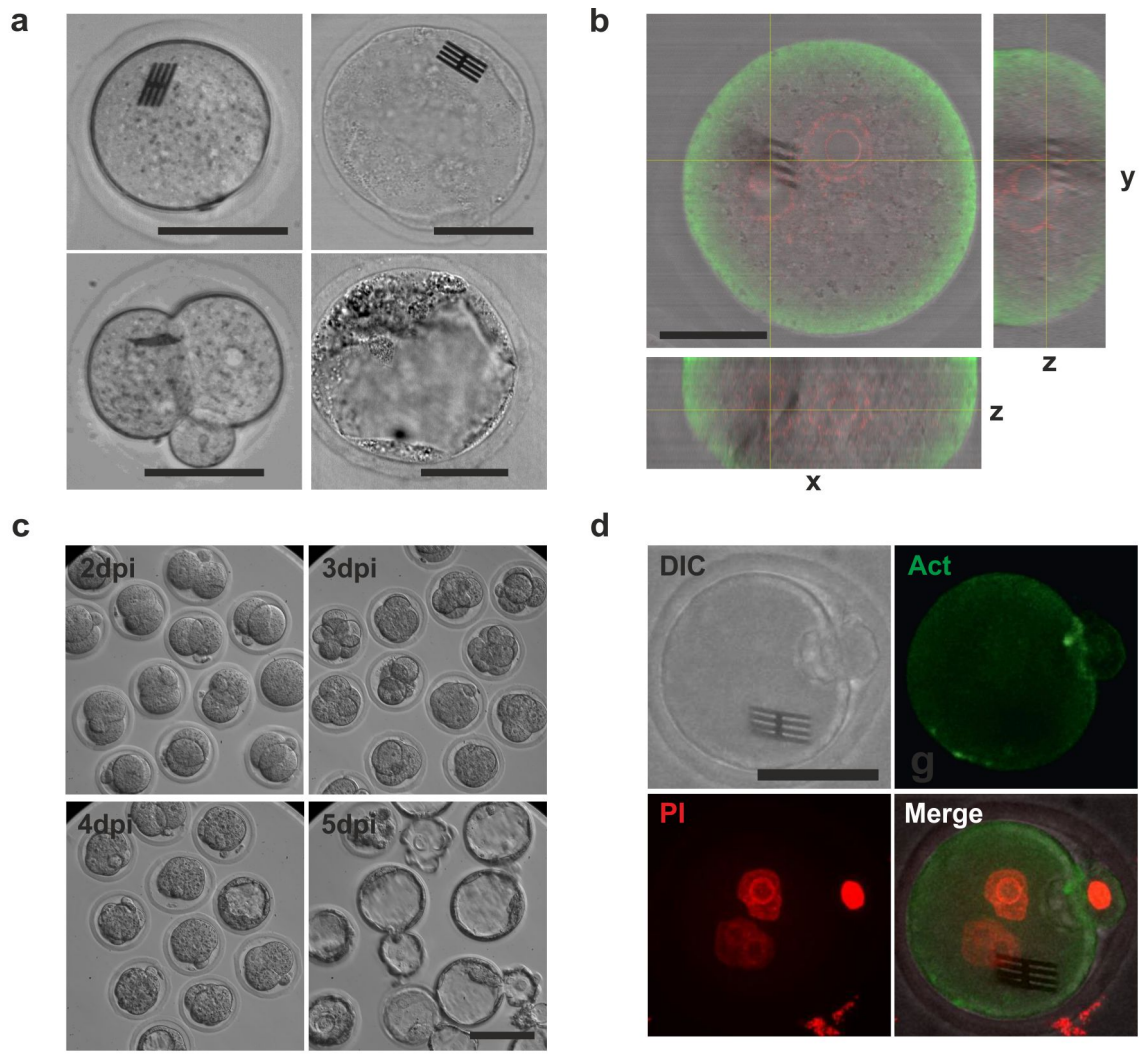
a
b
y
z
z
x
c
2dpi
3dpi
4dpi
5dpi
d
DIC
Act
PI
Merge

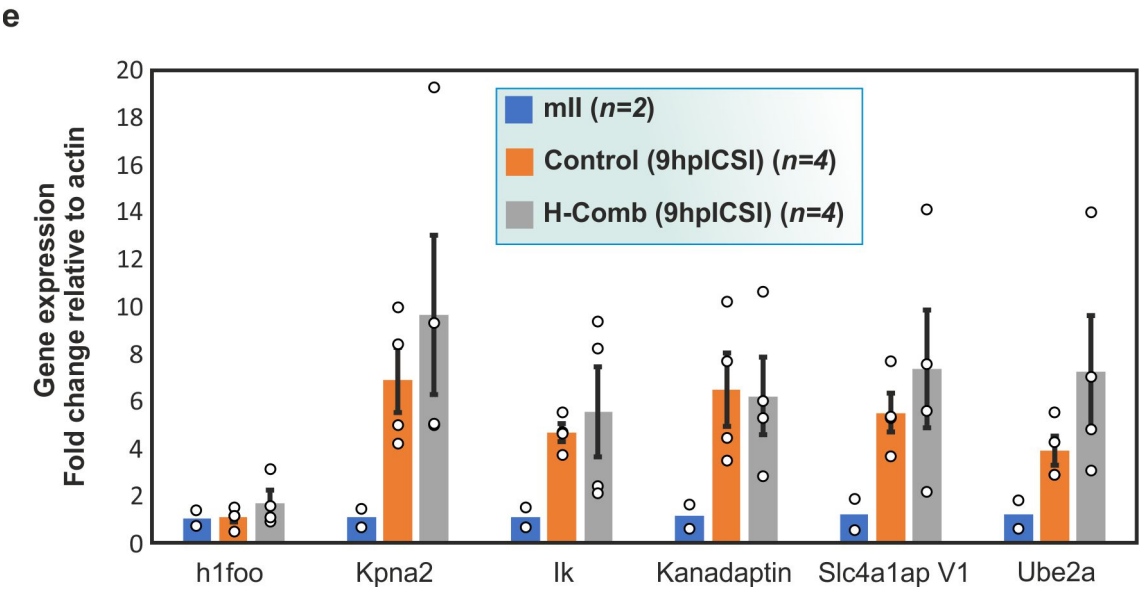
e
Gene expression
Fold change relative to actin
20
18
16
14
12
10
8
6
4
2
0
mII (n=2)
Control (9hpICSI) (n=4)
H-Comb (9hpICSI) (n=4)
h1foo
Kpna2
Ik
Kanadaptin
Slc4a1ap V1
Ube2a

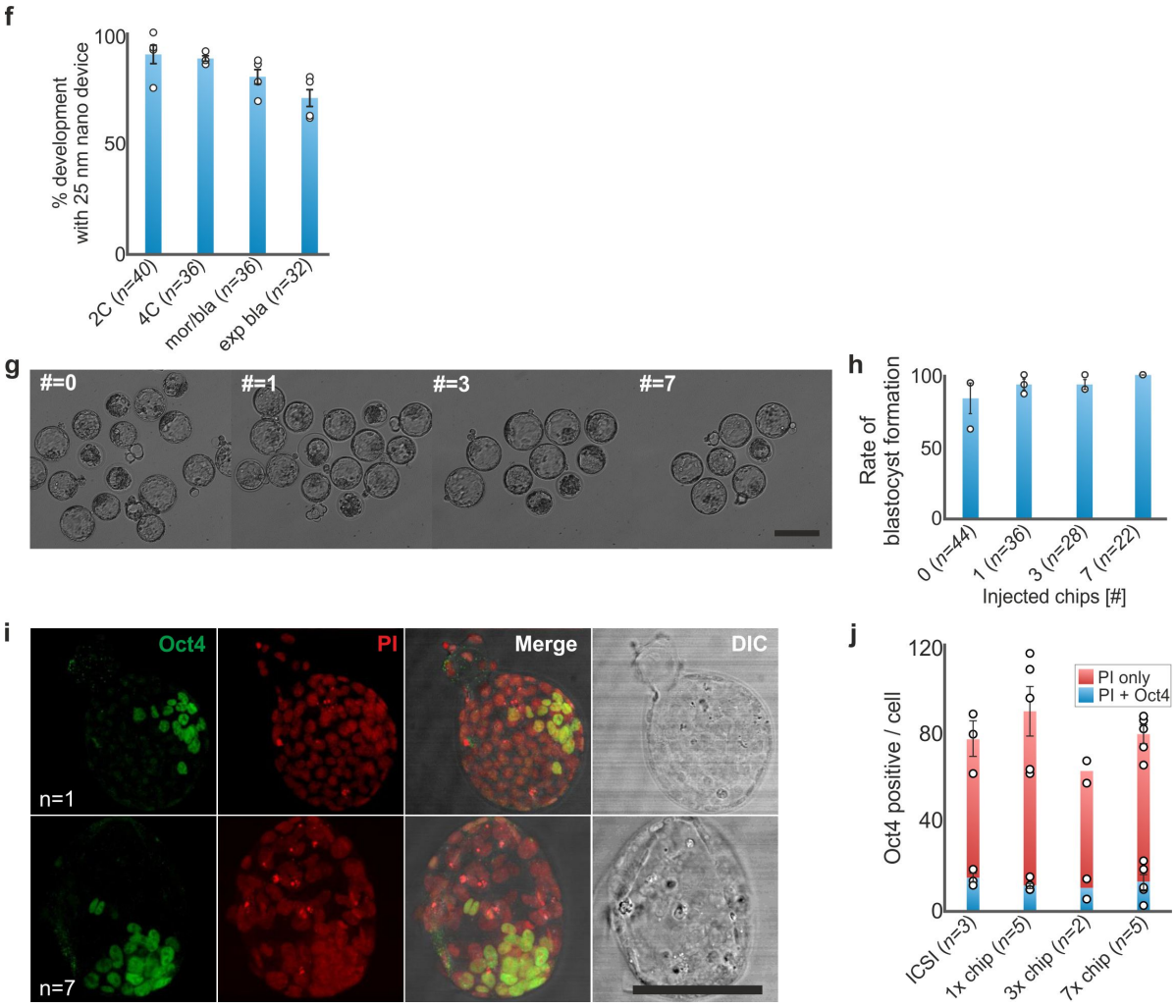

Supplementary Figure 10. Nanodevice behavior inside living mouse oocytes and during embryo development. **a,** Differential interference contrast (DIC) microscopy images of embryos after injection of sperm plus nanodevices of thickness 500 nm immediately (1 h) after injection (upper left) or in a blastocyst on embryonic day 4.0 (E4.0), *ie* four days after injection. Lower panels show analogous images collected at E1.5 (lower left) or at E4.0, but where the nanodevices were 50 nm thick; 50 nm nanodevices were not evident by E4.0. Scale bars, 30 μm. **b,** Confocal z-slices showing the cytoplasmic localization of a 25 nm nanodevice 6 h post-injection. Scale bar, 30 μm. **c,** Embryos containing H-comb nanodevices 25 nm thick at the indicated days post-injection (dpi). Scale bar, 100 μm. **d,** Confocal fluorescence

image of an embryo of (**c**) 6 h post-injection, labelled with Alexa 488-conjugated phalloidin (green) to visualize F-actin, and propidium iodide (red) to visualize pronuclear (genomic) DNA. Scale bar, 50 μm **e,** Histograms showing levels in one-cell embryos of transcripts that are upregulated following embryonic genome activation determined by ratiometric, semi-quantitative PCR (qPCR). Wild type metaphase II (mII) oocytes were injected with a sperm alone (n=4) or a sperm plus an H-comb device (n=4) and resulting embryos collected 8 h later. Transcript levels were normalized against levels of the house-keeping gene, *H1foo* and shown (± s.e.m.) relative to a value set at ~1.00 for mII oocytes. Unpaired two sided t-test p≥0.25 for all control *vs* corresponding H-comb embryo levels (*H1foo*, p=0.321; *Kpna2*, p=0.488; *Ik*, p=0.683, *Kanadaptin*, p=0.907; *Slc4a1apV1*, p=0.416; *Ube2a*, p=0.261). **f,** Development of 25 nm nanodevice-injected embryos plotted at two-cell (2C, n=40), four-cell (4C, n=36), morula-blastocyst (mor/bla, n=36) and expanded blastocyst (exp bla, E5.0, n=32) stages (± s.e.m.). Dot plots indicate percentages from n=4 biologically independent experiments. **g,** Embryo development *in vitro* to the blastocyst stage (E5.0) following initial coinjection of mII oocytes with sperm plus 0, 1, 3 or 7 test 3.0 x 3.0 x 0.025 μm nanosquares (chips) ($22<n<44$). The number of nanosquares injected per embryo is indicated in the upper left of each panel. Scale bars, 100 μm. **h**, Percentages (±s.e.m.) of starting embryos (n) of (**g**) developing to the blastocyst stage at E5.0 shown graphically. Dot plots indicate percentages from n=3 biologically independent experiments. **i**, Representative immunofluorescence confocal images of E5.0 blastocysts (n=8) generated by injecting sperm alone or sperm plus one or seven of the test silicon nanosquares of (**g**) as indicated. Labeling was of Oct4 (green) and nuclear DNA (propidium iodide [PI], red). Scale bar, 100 μm. **j**, Numbers of cells (± s.e.m.) in E5.0 blastocysts ($2\leq n\leq 5$) of (**i**) as judged by nuclear labeling with PI for the total, or those expressing Oct4 as judged by immunofluorescence with an anti-Oct4 antibody. *n*

refers to biologically independent samples throughout unless stated otherwise.

a

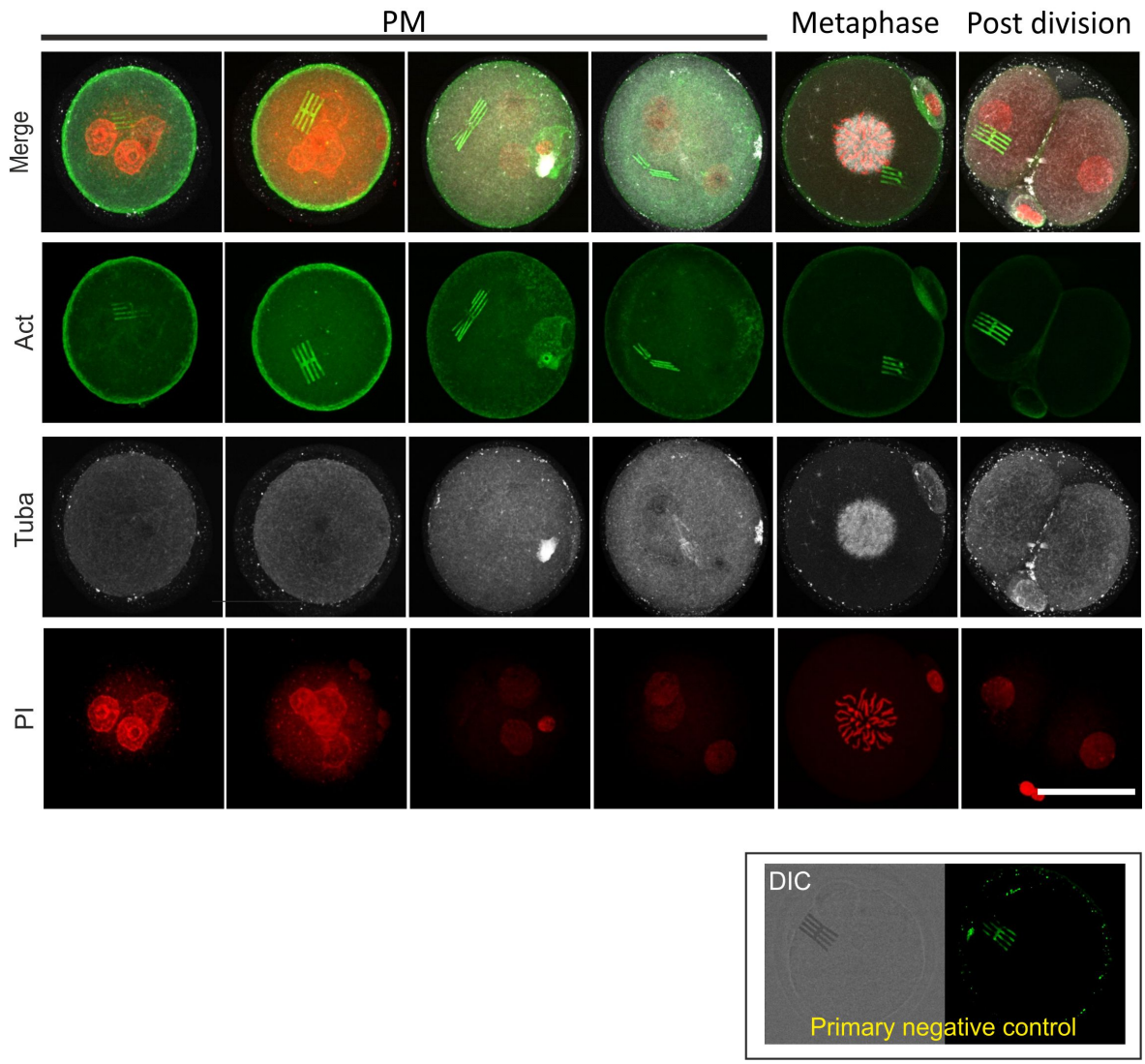
PM
Metaphase
Post division
Merge
Act
Tuba
PI
DIC
Primary negative control

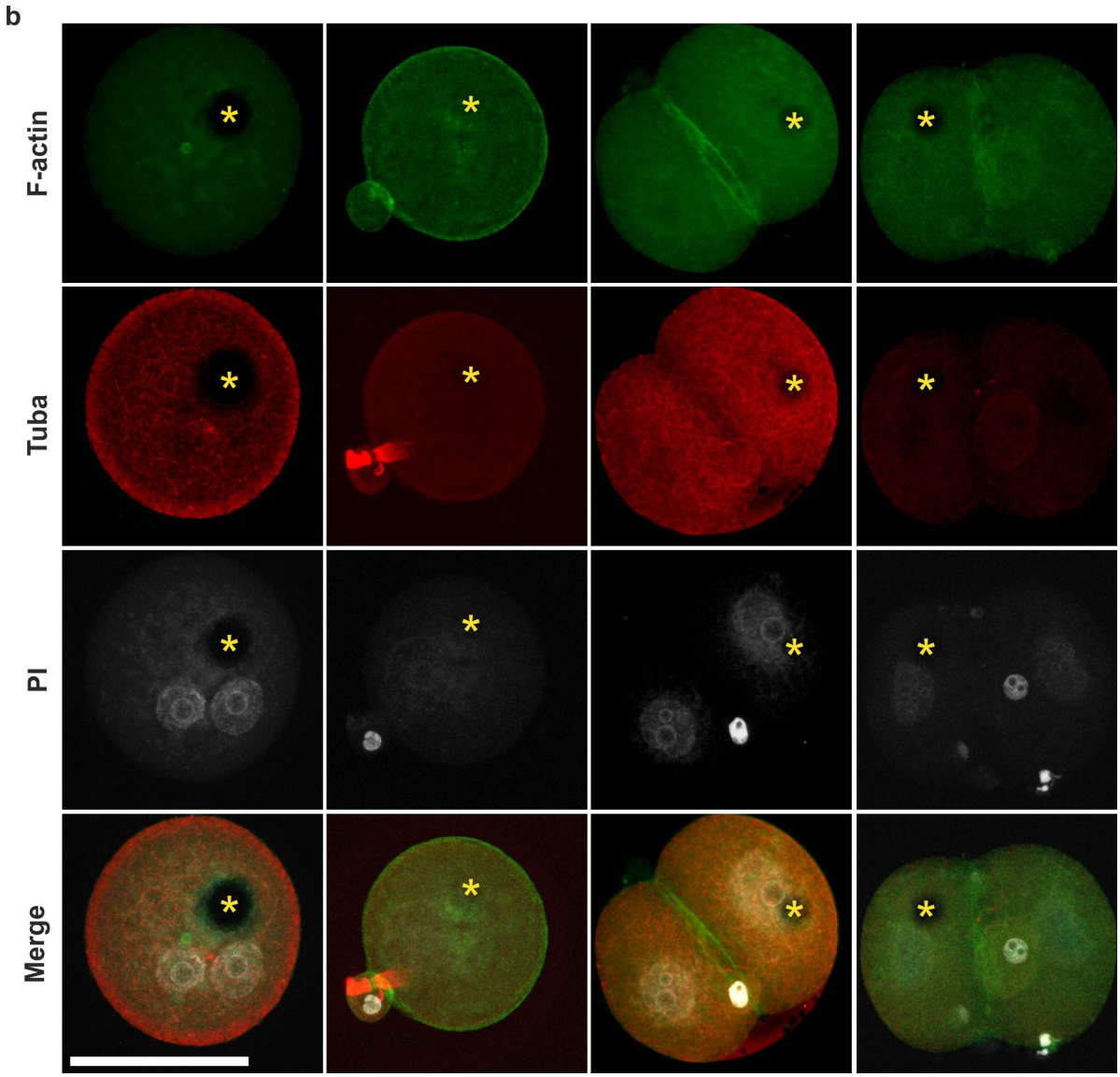
b
F-actin
Tuba
PI
Merge

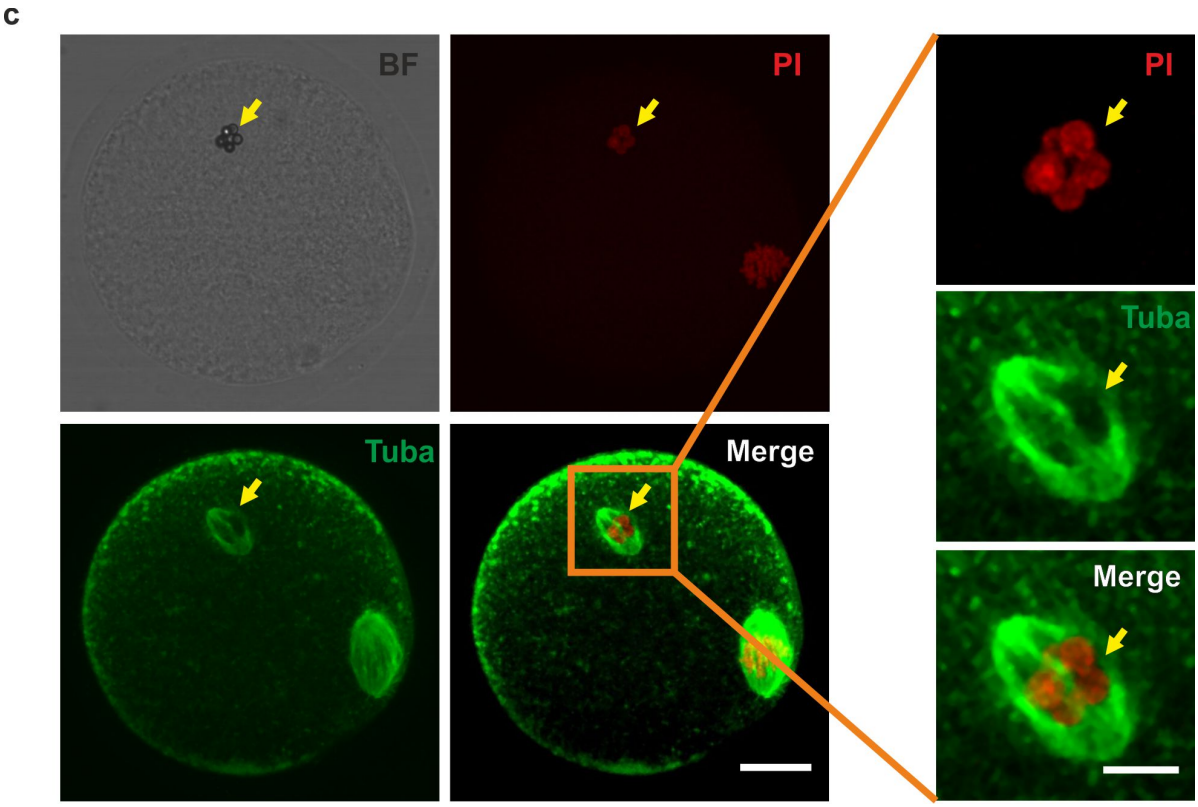

Supplementary Figure 11. No evidence for physical interaction between nanodevices or microspheres and the embryo cytoskeleton. **a,** Representative fluorescence confocal images of embryos 6 h after co-injection of a sperm head plus an H-comb nanodevice into metaphase II (mII) oocytes or 2-cell embryos (*n*=20 each). Embryos were stained with phalloidin to label F-actin (green), anti-α-Tubulin antibodies to label α-Tubulin (gray) and propidium iodide to label nuclear DNA (red). At this thickness (100 nm), nanodevices reflect light of the wavelength used (488 nm) and can be visualized without labelling. **b**, Fluorescence confocal images of embryo as per (**a**), except that a microsphere was coinjected with the sperm head (*n*=20). Asterisks indicate the positions of injected microspheres. Scale bar, 70 μm. **c,** Fluorescence micrographs of mII oocytes injected with DNA-conjugated latex microbeads[2] and stained 4 h later with anti-α-Tubulin antibodies to label α-Tubulin (green) and propidium iodide to label nuclear DNA (red). BF, bright field. Scale bars, 10 μm, and

20 μm (insets). *n* refers to biologically independent samples obtained over two biologically independent experiments.

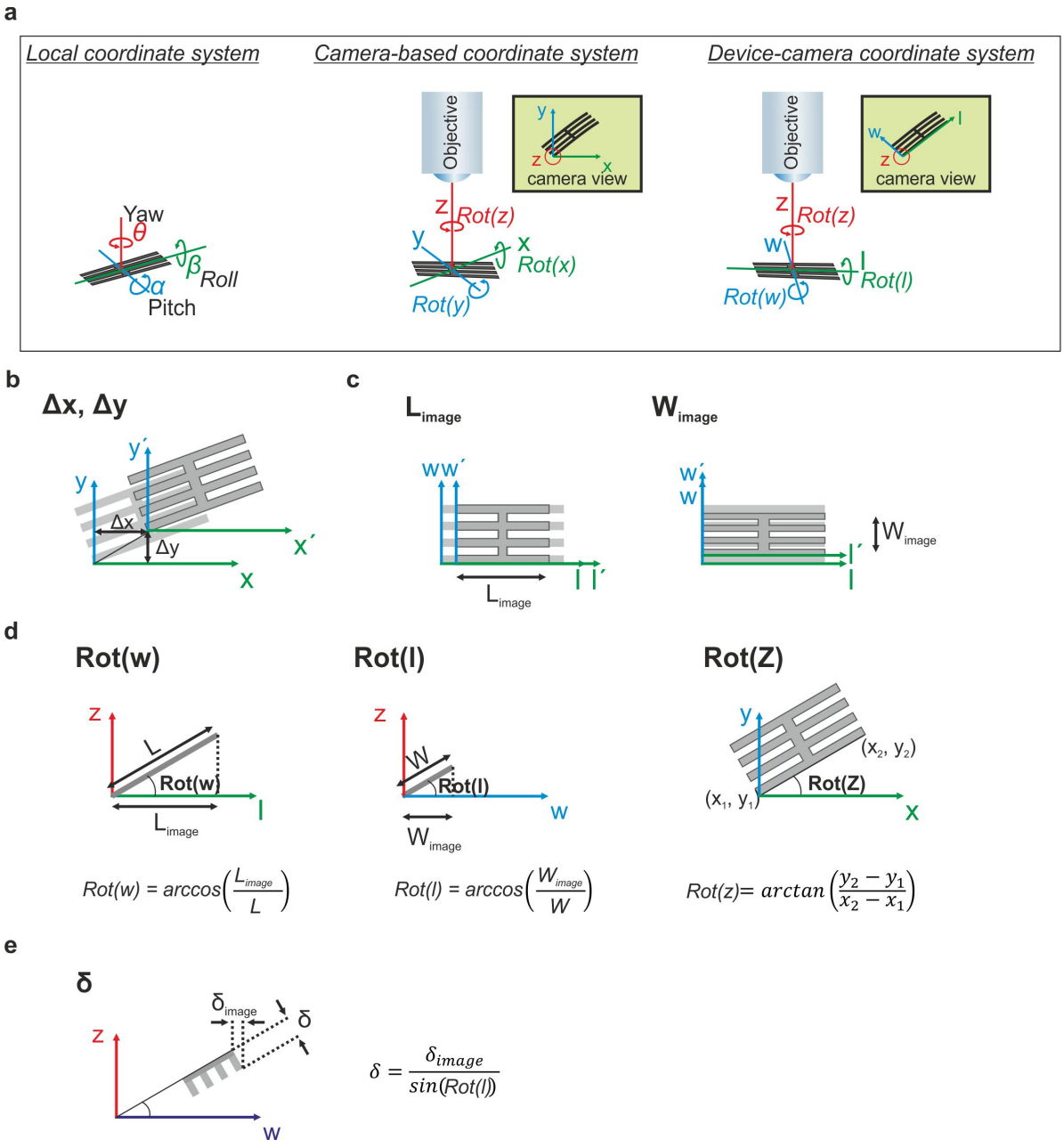

Supplementary Figure 12. Translation, rotation and deformation formulas. The mechanical performance of nanodevices inside embryos was determined by their geometrical parameters, obtained from movies using ImageJ analysis software (http://rsbweb.nih.gov/ij). All values were obtained in pixels and translated to appropriate units considering the image acquisition parameters. **a**, Coordinate systems based on the device (left), on the camera view (center) and on the axis aligned to the long axis of the device, the axis aligned to the short

axis of the device and on the axis of the objective. For reduced Rot(w) and Rot(l), most data processing approximated closely to these conditions; the device-camera systems is similar to the device coordinate systems. **b**, Schematic showing the 2D-translation of the device. Δx and Δy respectively define translations on x and y axes. **c**, Schematic showing the projected nanodevice length, L_{image}, and width, W_{image}, in the plane of the image. These parameters are required to calculate changes in device orientation and deflection. **d**, Schematics of nanodevice rotations Rot(w) (left), Rot(l) (center) and Rot(z), with the corresponding formulae for their respective calculations given underneath each. **e**, Schematic and corresponding formula for the calculation of nanodevice deformation, δ.

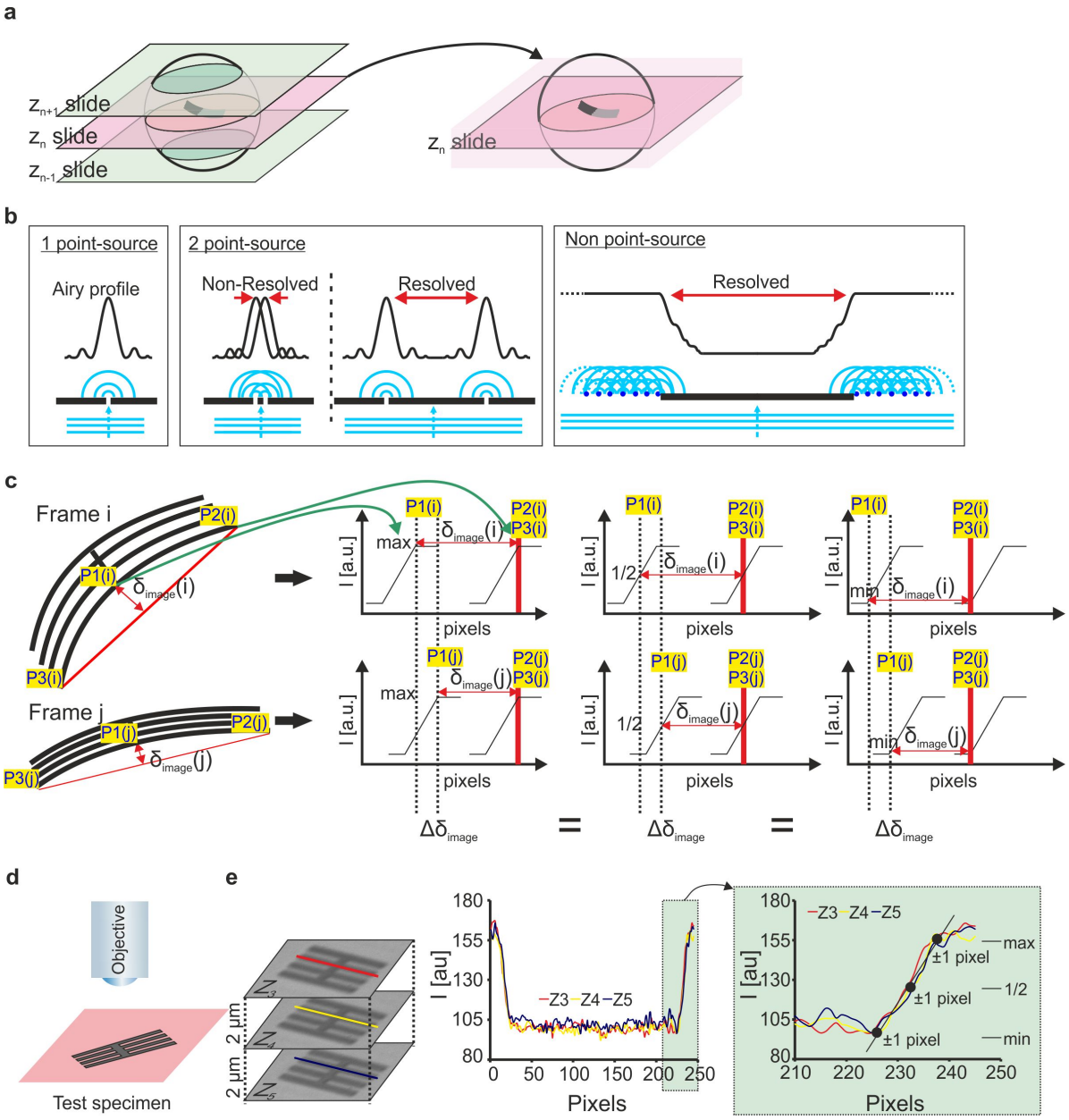
a
z_n+1 slide
z_n slide
z_n-1 slide
z_n slide
b
1 point-source
Airy profile
2 point-source
Non-Resolved
Resolved
Non point-source
Resolved
c
Frame i
P1(i)
P2(i)
P3(i)
δ_image(i)
Frame j
P1(j)
P2(j)
P3(j)
δ_image(j)
I [a.u.]
max
1/2
min
pixels
Δδ_image
=
d
Objective
Test specimen
e
Z3
Z4
Z5
2 µm
2 µm
I [au]
180
155
130
105
80
0
50
100
150
200
250
Pixels
Z3 Z4 Z5
max
±1 pixel
1/2
±1 pixel
min
±1 pixel
210
220
230
240
250

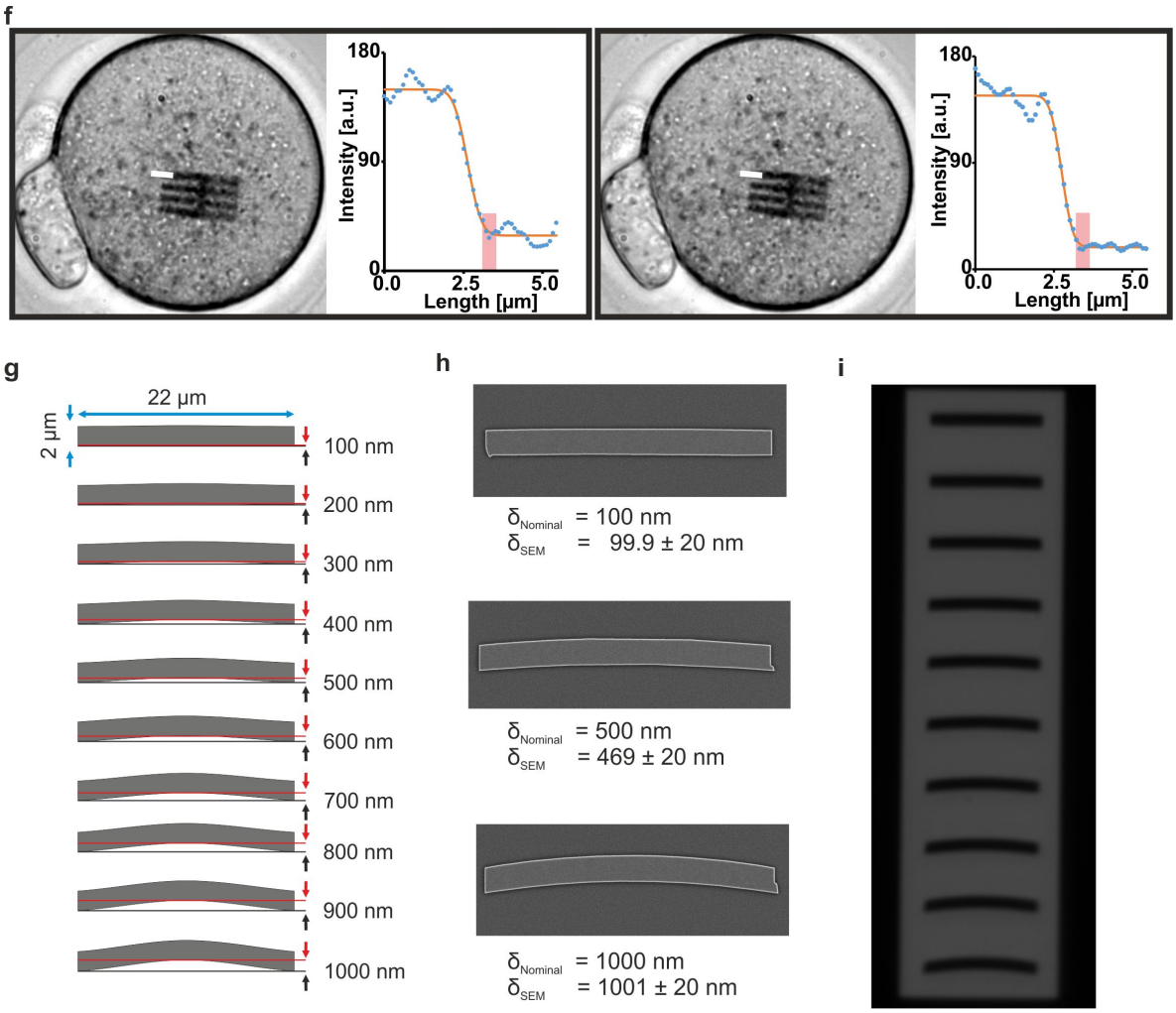

j

δ_{SEM} [nm]	100	141	258	398	469	586	656	791	908	1001
$\delta_{Optical}$ [nm]	103	132	210	315	406	511	609	702	850	1022
δ_{SEM}-$\delta_{Optical}$ [nm]	-3	9	48	83	63	75	47	89	58	-21

Supplementary Figure 13. Algorithm for deflection calculations. **a**, Representations of z-stack images (left) corresponding to those taken for videos. The best-focused images (right) are used for processing. **b**, Resolving dimensions. The resolution of an optical microscope is constrained by light diffraction. A point source of light, or light passing through a minute space (left), appears in the images as a small pattern (so-called 'airy patterns') and not as a point. Thus, the optical resolution of a microscope (center) is defined as the smallest distance between two points on a specimen that can still be distinguished as two separate entities.

Without computational fitting algorithms, this limits the smallest distance between two points that can be distinguished to a few hundred nanometers. However, if the two image points are far enough apart, they can be recognized as separate objects and their separation can be calculated even though they cannot be individually resolved. When there are non-punctate light sources (right), as in the case of light passing near to the nanodevices, it follows from the Huygens-Fresnel principle that each point on a wave-front is itself a source of spherical wavelets. The sum of these spherical wavelets forms the wave-front, which can be viewed as the origin of the diffraction effects on their borders. **c**, To calculate the device deflection, δ_{image}, we draw an imaginary line (red) on the image. The distance, δ_{image} is the smallest that is determined. However, we took advantage of the fact that here, it is not necessary to resolve features and that all devices have an offset bending. As devices can be tilted (rotation), for the determination of the position of each point of the device required for the measurements [labelled P1, P2, P3 in (**c**)] we selected the best-focused z-slide for each one, which is not necessarily on the same focal plane. **d**, For image acquisition, we obtained 7-10 z-slices; adjacent optical slices were separated by 2 μm (z-step). We calculated errors in the determination of distances between adjacent slices using a flat dummy device as a test specimen, deliberately out of focus in +1 and -1 z-planes. To achieve this, devices immersed in ethanol were deposited onto glass such that after the ethanol had evaporated, the chip adhered to the glass slide, assuring its flatness and avoiding device rotation before the seven images were acquired. **e**, Extracted images (left) from a z-stack comprising seven optical sections each with a 2 μm z-step, showing the high contrast of a nanodevice, whether the device is in focus (Z_4) or out of focus (Z_3 and Z_5). Colored lines depict the line-ROI (region of interest) for intensity profile plots. Intensity profile plots (center) of line-ROIs, showing that even when the devices are out of focus (±1 optical slice), the dimensions extracted from

their intensity profiles are similar. Detail (right) of the same profile taken from the border of the chip, where diffraction and noise effects are observed as a gradual intensity transition in spite of the step transition. Black dots indicate the pixel ratio ±1. Although best-focused z-stack images are used for dimension processing, points not exactly in the focal plane can also be measured accurately. The main contribution of defocusing (blurring) occurs when there is a lack of contrast, but as silicon is opaque, the contrast of the nanodevices in the images is very high, facilitating image processing. Diffraction is not the main limitation for the determination of δ_{image} as long as the same criteria are always used to calculate it (max, half or min intensity; see also **c**) to localize pixels P1, P2 and P3 at the borders of the nanodevice. On the contrary, the optical noise inside the embryos is the main limitation for the deflection calculation; we accordingly indicate low confidence at magnitudes <0.5 μm as a grey area in Figures 2d and 6f. **f**, Optical images of a mouse embryo containing a microinjected H-comb nanodevice (left in each pair), showing the optical profile (along a path indicated by white lines in each micrograph) at the edge of the nanodevice (right in each pair) at two time points during videomicroscopy. For processing of P1, P2 and P3 we used the minimum values of the diffraction profile (indicated with a pink rectangle). **g**, Optical test structures designed to confirm that measurements below the diffraction limit are possible. To verify the precision in the method we used to calculate cantilever bending, δ, we tested structures that were designed to capture nanodevice bending statically. The set of structures comprised 10 bars with bending of 100 nm to 1000 nm in 100 nm increments. **h**, Scanning electron microscope (SEM) images of the fabricated devices showing their intended bending ($\delta_{nominal}$) and the bending determined empirically by SEM (δ_{SEM}). Technology based on electron beam lithography permitted fabrication with nanometer precision and SEM inspection allowed accurate determination of object dimensions before they were subsequently used as test

specimens. **i**, Optical images (60 x objective) of the test structures. Once calibrated by SEM, test structures were used to confirm the fidelity of bending determination by optical microscopy. **j**, Calibration values of δ_{SEM} and $\delta_{Optical}$ determined by optical microscopy for each test structure, showing the $\delta_{Optical}$ errors assuming the δ_{SEM} as calibrated values. $\delta_{Optical}$ errors were below the 2 pixel error that we considered for our calculations. The main source of errors in our method to determine δ is due to the optical noise inside the embryo and is not limited by diffraction.

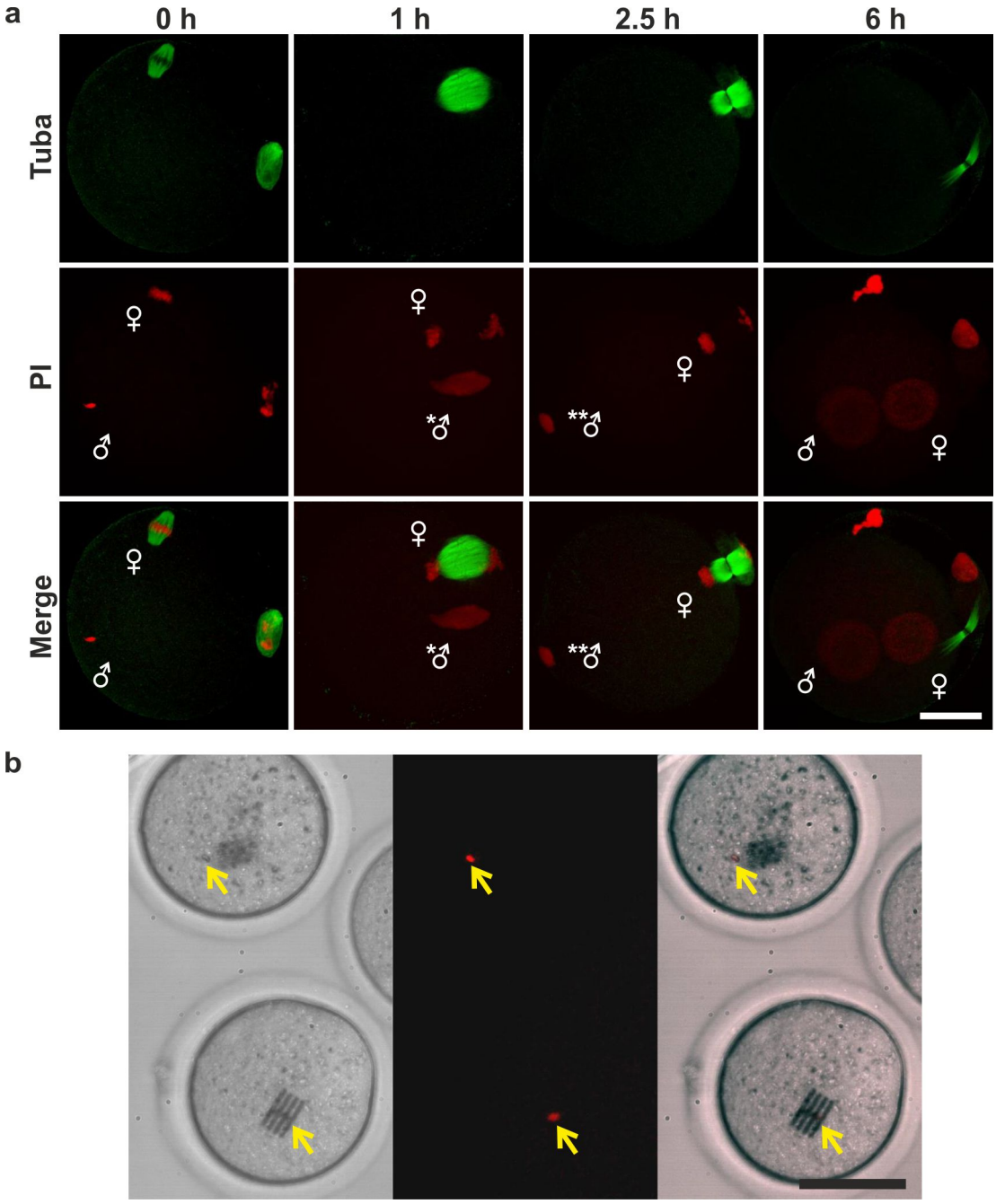

Supplementary Figure 14. Sperm decondensation and recondensation (SDR-phase) immediately after fertilization. **a,** Representative confocal fluorescence micrographs of embryos (*n*=3 biologically independent experiments) at the times indicated after sperm injection (ICSI), stained for α-Tubulin (green) and with propidium iodide for nuclear DNA (red). Sperm chromatin decondenses (*) and then recondenses (**) prior to pronucleus

formation. Scale bar, 20 μm. **b,** Sperm from homozygous *Prm2-mCherry* transgenic male[2]. Coinjection typically proximated nanodevices to within ~10 μm of sperm (n=4 biologically independent samples). Scale bar, 50 μm.

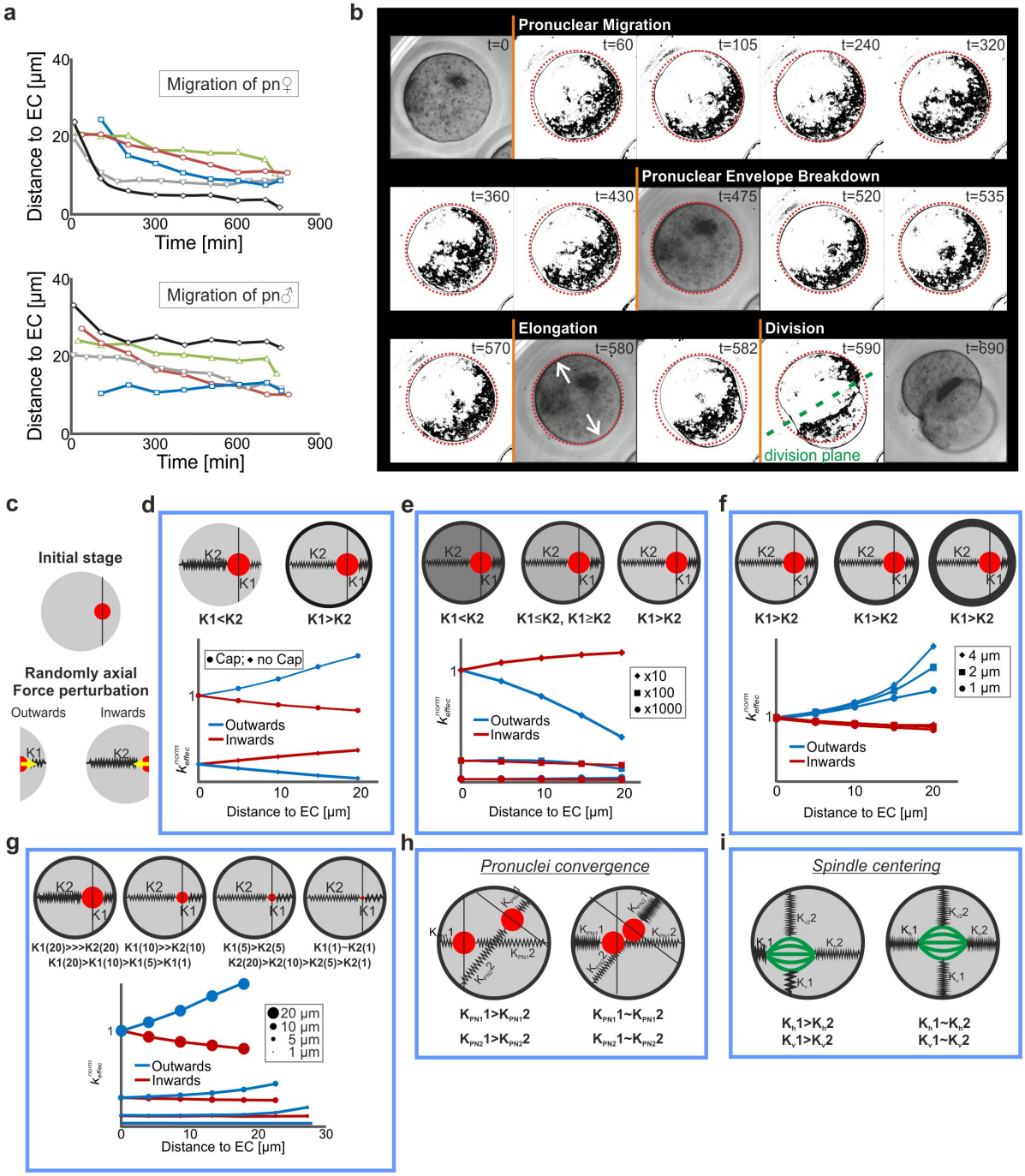

Supplementary Figure 15. Embryo dynamics and predictive GES model for the pronuclear migration (PM) phase. **a,** Distance to the center of the embryo *versus* time, shown for female (upper) and male pronuclei. Data were extracted from 2D images. Pronuclei apparently migrated more rapidly towards the embryo center when they were closer to the embryo periphery (cortex). Pronuclei nearer to the center stopped or decreased their

centring speed ahead of pronuclear membrane breakdown. These results are consistent with previous reports[3]. **b,** Bright-field images showing membrane ruffling during pronuclear migration (PM), embryo elongation (EL) and division (DIV) phases in diploid one-cell embryos. During pronuclear convergence, the plasma membrane underwent dynamic ruffling on a scale of ~2 μm. Ruffling rapidly arrested on pronuclear membrane breakdown and was absent during embryo elongation and one-to-two-cell division. n=5 biologically independent experiments in (**a**) and (**b**). **c,** Effective rigidity experienced by a spherical object (*i.e.* pronucleus) to a small axial force perturbation within a larger sphere (*i.e.* embryo). The spherical object was considered to behave like a solid that was not fixed in the cytoplasm and which could only apply pushing forces (compression) towards the cytoplasm. Thus, only the sphere region under compression is modelled in each case. **d,** The model predicts that smaller spherical objects experience different stiffness when they are forced to move towards the inside or towards the edge of the embryo, implying that for random-force perturbations, the spherical objects will move towards the edge in the absence of a relatively rigid cap. On the contrary, in the presence of a rigid cap (*ie* membrane-plus-cortex system), the spherical object is predicted to move to the center of the sphere. The difference between inwards and outwards effective rigidity depends on (**e**), the ratio between the stiffness of the cortex (mechanical properties and tensioning) and of the sphere (mechanical properties of the cytoplasm), in addition to (**f**), the thickness of the cortex. **g**, The difference in effective stiffness (K_{eff}) also depends on the spherical object diameter. Thus, large spherical objects experience a more rigid environment in which to move than do the smaller ones. However, their inwards:outwards effective rigidity ratio is larger, which means that for this model, large particles are predicted to move towards the center (model with a stiffer cortex) when they are subjected to a random force. Particles that are very small relative to the embryo will have no

preferable direction of motion. **h,** The model explains pronuclear convergence to the center of normal diploid embryos. **i**, GES also accounts for posterior spindle centring. Solid-liquid cytoplasmic duality in zygotes due to soft solid organelles, filamentous structures, intra-embryonic fluxes and the existence of two large subcellular objects (the pronuclei themselves) could also affect pronuclear centralisation. In addition, differences in inwards-outwards effective rigidity are so small that centring might be affected if electrostatic charges or directional forces between the pronuclei were involved in pronuclear convergence and spindle centring. Panels (**c-i**) concern the relevance of boundary conditions when the mechanobiology of the cytoplasm is described by elastic, viscous or viscoelastic conditions. If they are not considered, the effective rigidity and viscosity of the cytoplasm can be underestimated.

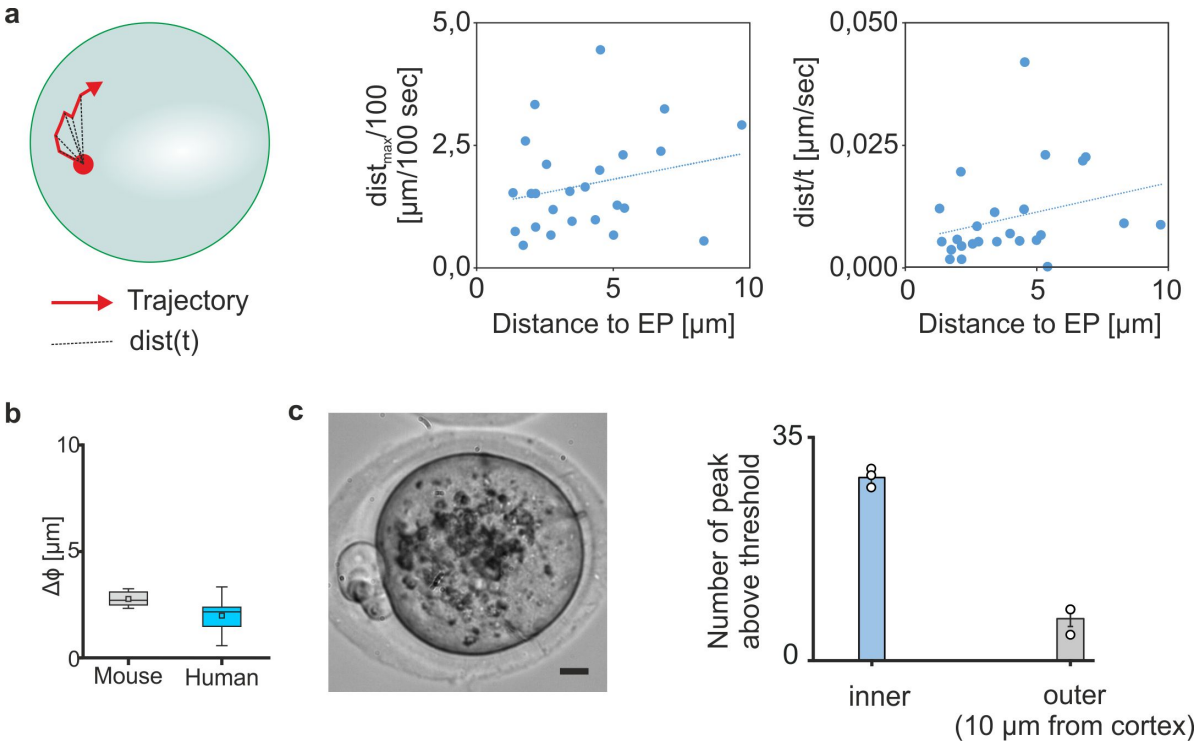

Supplementary Figure 16. Endogenous embryonic behavior corroborates the GES model. a, Schematic (left) representing the trajectory (red) of an endogenous particle within a one-cell mouse embryo, and the distance (*dist*) from its starting position (black). Empirical analysis of real time movies (center) allowed optical tracking of particles (1.9-6.9 µm diameter; average 2.8 µm) within living embryos (n=3 biologically independent samples (embryos); ~2 h post-fertilization) so that their respective maximum distances could be plotted from the starting position, $dist_{max}$ (normalized to 100 seconds) *versus* the particle distance from the embryo periphery (EP). Plots are shown (right) for distances from the respective starting positions of particles over a given time, relative to their starting positions from the embryo periphery. Particles within ~10 µm of the membrane border were analyzed, as this is the region in which GES is relevant for particles with diameters in the 1.9-6.9 µm range (Fig. 3f). Linear fitting with straight lines is included to approximate tendencies. Particles close to the embryo periphery exhibited relatively small maximum displacements,

in agreement with GES model. **b**, Increase in pronuclear diameter during the PM-phase for mouse and human one-cell embryos. Note that for human embryos, data were recorded only for the last 3 h of the PM-phase; the increase over the entire PM-phase is therefore expected to be larger. *n*=5 (mouse) and *n*=10 (human) biologically independent samples (embryos). Data are box-and-whiskers plots (whiskers, from 0 to 99th percentile; box, from 25th to 75th percentile; line within the box, median). Values for maximum, mean and minimum are for mouse, 3.26, 2.78 and 2.34, and for human, 3.33, 2.00, 0.57. **c**, Bright-field micrograph (left) of one-cell 129/SvJ embryos indicates that larger particles tend to be located away from the embryo periphery. A corresponding histogram (right) plots average peak (*ie* particle) number in standardized selected areas of one-cell 129/SvJ embryos areas (*n*=3 biologically independent samples [embryos]). Values (± s.e.m.) are significantly higher (unpaired two-sided *t*-test, *p*=0.000377) for embryo interiors ('inner') than the cortical region ('outer'). Scale bar, 10 μm.

a

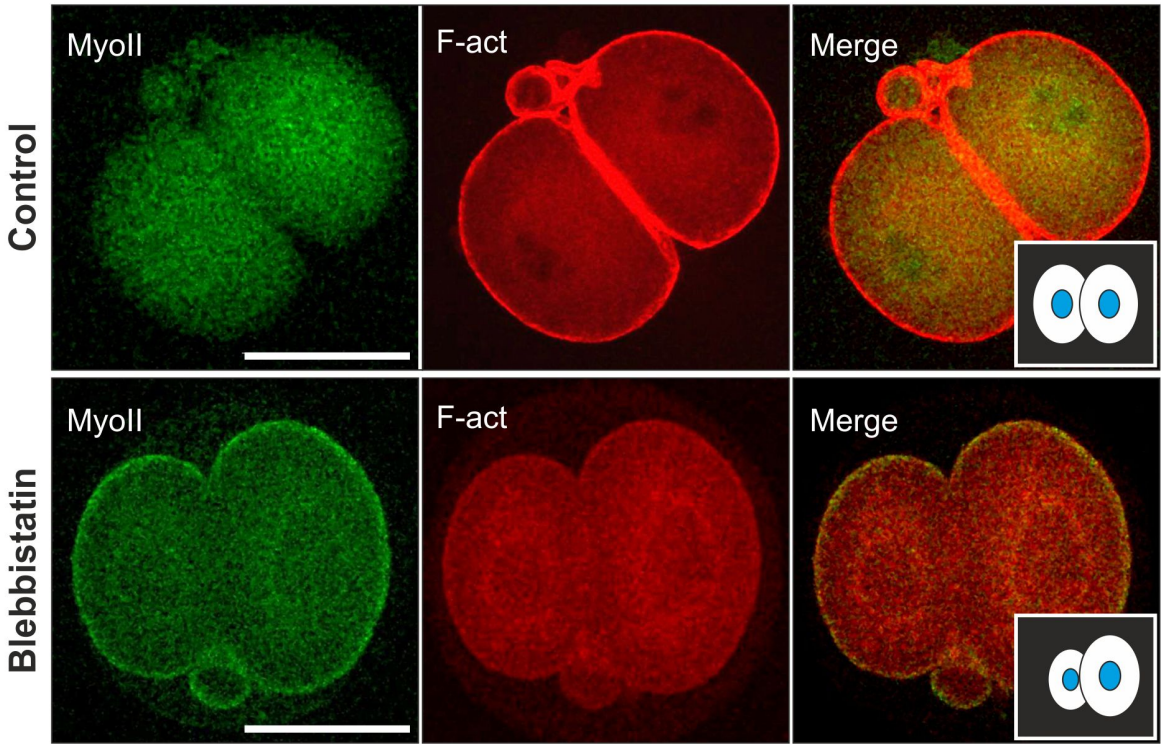

Supplementary Figure 17. Mechanical perturbation of one-cell embryos by inhibiting actomyosin with blebbistatin. **a,** Representative vertically paired fluorescence confocal images of two-cell embryos following culture in the presence (lower; *n*=12) or absence (control, *n*=20) of the myosin (actomyosin) motor inhibitor, blebbistatin (200 μM). Embryos were stained with phalloidin to label F-actin (red) and anti-MyoII antibodies (green) to label actomyosin. Images show z-projections of embryos, with (insets) corresponding to schematic representations. Exposure to blebbistatin treatment did not prevent cell division *per se* but tended to reduce levels of F-actin at the embryo cortex and induce asymmetric division. Scale bar, 50 μm. *n* refers to biologically independent samples obtained in each case over two biologically independent experiments.

Supplementary Movies

Supplementary Movie 1. Animation of the axis of rotation of the nanodevice. Movie depicts nanodevice rotation axis and angles. *Rot(l)* denotes a rotation around the *l*-axis, *Rot(w)* denotes a rotation around the *w*-axis and *Rot(z)* denotes a rotation about the *Z*-axis.

Supplementary Movie 2. Brightfield movie of mouse zygote during pronuclear migration. Movie shows representative cortical membrane ruffling during pronuclear convergence (PM-phase) in embryo starting ~6 h after sperm injection into wild-type metaphase II oocyte. *n*=48 biologically independent samples obtained over eight biologically independent experiments.

Supplementary Movie 3. Brightfield movie of mouse zygote containing microsphere. Representative brightfield movie of an embryo produced following injection of wild-type metaphase II oocyte with microsphere (bead) plus a sperm head, showing bead trajectory from pronuclear formation (PF) to the end of the pronuclear migration (PM) phases. *n*=13 biologically independent samples obtained over two biologically independent experiments.

Supplementary Movie 4. Tracking particle migration within an embryo. Movie depicting migration of particles within mouse embryos ~2 h after fertilization, in the presumptive SDR-phase. Particles exhibiting processive migration tend to migrate least the nearer they are to the periphery. *n*=31 biologically independent samples obtained over three biologically independent experiments.

Supplementary Movie 5. Dynamic surface plot of Utrophin-mCherry in mouse embryos. Oocytes pre-injected with cRNA encoding Utrophin-mCherry were then injected with sperm and fluorescence intensity monitored during culture, here shown for a cohort of

embryos (left) and a single embryo in detail. Note that the second polar body can contribute to fluorescence if it is situated in the center of the embryo field of view.

Supplementary Movie 6. Fluorescence in mouse embryos containing Utrophin-mCherry. Oocytes pre-injected with *Utrophin-mCherry* (Utr-mCherry) cRNA were then injected with sperm and fluorescence recorded during one-cell embryo culture. Surface ruffling occurs with the formation of a Utr-mCherry cloud around pronuclei during pronuclear migration (PM-phase). This ruffling stops precipitously upon pronuclear envelope breakdown (PEB); there is apparently coordinated rapid disappearance of the cloud, appearance of cortical Utr-mCherry and cessation of surface ruffling. n=4 biologically independent samples.

Supplementary Movie 7. Brightfield movie of mouse embryo containing 25 nm 'H-comb' nanodevice. Representative brightfield movie of an embryo following injection of a wild-type metaphase II oocyte with a 22.0 x 10.5 x 0.025 μm 'H-comb' nanodevice plus a sperm head, showing nanodevice behavior in the resulting elongation (EL) phase embryo. n=48 biologically independent samples obtained over eight biologically independent experiments.

Supplementary Movie 8. Brightfield movie of 'scary spider' mouse embryo containing 25 nm 'H-comb' nanodevice. Representative brightfield movie of an embryo following injection of a wild-type metaphase II oocyte with a 22.0 x 10.5 x 0.025 μm 'H-comb' nanodevice plus a sperm, showing nanodevice behavior (and FEM simulation) at the division phase (DIV) of the resulting embryo. n=2 biologically independent samples.

Supplementary Movie 9. The effect of actomyosin inhibition is consistent with the GES model. Representative brightfield movies of embryos (n=3) cultured in the presence (right)

or absence of the myosin inhibitor, blebbistatin, during the pronuclear migration (PM) phase. Embryos treated with blebbistatin undergo decreased membrane ruffling. Since blebbistatin is an inhibitor of the motor protein, myosin II, this suggests that surface ruffling is a consequence of actomyosin contraction[4]. This cytoplasmic mechanical load reduction is reported by nanodevices deep inside embryos (pressure or forces; Fig. 6g). Whilst exhibiting decreased membrane ruffling and cytoplasmic forces, the embryo treated with blebbistatin also undergoes larger oscillations of relatively large cytoplasmic structures (including pronuclei). This is in agreement with a role for actomyosin in the control of cytoplasmic stiffness; reducing actomyosin consequentially reduces cytoplasmic stiffness. The final situation is that a pn moving to the center is largely affected (Fig. 6b) due to a reduction of the mechanical loads. In this video, pronuclei do not migrate to the center of blebbistatin-exposed embryos during the PM-phase, but move outwards, towards the embryo cortex. We reason that this is because there is a reduction of cytoplasmic stiffness, and hence the ratio of the resistance to move outwards or inwards is reduced, delaying pronuclear centring, but there is probably also a contribution from membrane stiffening, an additional consequence of actomyosin inhibition[5], also in agreement with the GES model. The GES model predicts that a gradient of effective stiffness within a relatively stiff cortical shell helps to propel pronuclei to the embryo center, so reducing this stiffness - one predicted consequence of inhibiting the cytoskeletal component, actomyosin - abrogates pronuclear migration to the embryo center. Moreover, a soft cytoplasm is expected to increase random pronuclear movement, further disrupting pronuclear centring. *n* refers to biologically independent experiments.

Supplementary Discussion

A putative gradient of effective stiffness, GES, for pronuclear centring

It has previously been proposed that actin-positive foci moving at uniform speed but distributed non-uniformly in mouse embryos produce a pressure gradient (∇P) such that the larger any object within the embryo (*e.g.* a pronucleus, pn), the greater its speed[3]. This model is in agreement with our experimental observation that pronuclei and nanodevices tended to approach the center (Fig. 3d). However, the surface of the embryo also experienced random displacements that were of a similar magnitude and with apparently similar kinetics to displacements experienced by nanodevices near to the embryo center (Fig. 3c). One interpretation of this is that non-inertial forces move nanodevices (and pronuclei) at the embryo center. These forces, acting throughout the cytoplasm, link surface and internal displacements. However, when we tested this further by microinjecting microspheres, we found no correlation between microsphere size and speed (Fig. 3e); this behavior is not accounted for by a force gradient model alone[3].

To account for pn centralization, we suggest that a gradient of effective stiffness (GES), effective elastic constant and viscosity, exists throughout the embryo. As a first approximation, the cytoplasm of the embryo can be modelled as a simple combination of elastic and viscous elements, approximations that have commonly been used to fit cell mechanics data[6]. These cannot describe precisely the mechanical behaviour of the cytoplasm, but they have been used to extract material science results relevant for cell mechanobiology.

The GES model predicts that a growing object inside the embryo will migrate towards the embryo center, where the effective stiffness is lower. Indeed, we observed that mouse

pronuclei expanded during the PM-phase (Fig. 3h) and expansion was also observed in videos of human embryos.

Based on the assumptions that the elastic contribution is greater in the direction of the displacement, inducing a smaller effective stiffness when moving towards embryo center, and that random forces of similar magnitude operate throughout the embryo (supported by evidence described above), the overall effect could contribute to pn centralization (Fig. 3i,j).

The GES model is consistent with more rapid centralization speeds the closer objects are to the embryo periphery (Fig. 3f, j). Microspheres did not always centralize (Fig. 3d) and additional factors that do not act upon microspheres may contribute to pronuclear localization. The GES model predicts that microspheres are out-competed by larger pronuclei for the embryo center, which is what was observed (Fig. 3d,k). As a test of this, we injected microspheres into embryos lacking pronuclei (Fig. 3k). In the absence of competing pronuclei, the microspheres tended to move to the center, consistent with the predictions of the GES model.

Since the GES model is related to intracellular effective stiffness, it is compatible with models of other attractive forces operating between the pronuclei, and even with mechanical load gradients. In addition, GES accounts for the displacement of other organelles (*e.g.* spindle centering).

Limitations and implications of the GES model

Elastic and viscous models have commonly been used to fit cell mechanics data generated from other experimental systems[6], but like these models, the GES model is descriptive in nature, as it assumes that the embryo interior is homogenous. However, cytoplasm within the embryo is heterogeneous and composed of organelles and an adaptive cytoskeleton that confound efforts to obtain exact analytical solutions. Accordingly, and due to this

heterogeneity, the GES model is restricted to predicting the tendency of large objects to centralize, but it cannot provide exact solutions for pronuclear displacement. Conversely, the GES model also reveals limitations in descriptions of cytoplasmic material behaviour using simple elastic and viscous models that do not consider how boundary conditions affect cytoplasmic effective mechanical properties; GES shows that the effective stiffness of the cytoplasm will depend, from a mechanical point of view, on the proximity of relatively stiffer regions (a stiffer cortex).

Cytoplasmic softening and the largest forces are manifest during the first cell division

Cleavage furrow progression is predicted rapidly to induce a shear stress and in consequence generate forces of high magnitude inside the dividing embryo. These predictions were supported by our data (Fig. 2e,f, right, Fig. 5e,f and Supplementary Movie 8). Their predicted consequence is to rearrange the cytoplasm on a large intracellular scale, as was revealed by the highest devices rotations (Fig. 2c). Even though DIV lasted only a few minutes, nanodevices underwent maximum rotations (for the entire one-cell history) of up to 137±2°, and maximum deformations of 4.2±0.3 μm (Fig. 2c,d), corresponding to pressures of 233±20 Pa (17.7±1.5 nN) (Fig. 2e). This mechanical activity was approximately two orders of magnitude higher than at any other time in the embryo (Fig. 2f, right). We noted that nanodevices within mouse embryos (which lack a dedicated aster-based system for pronuclear centering), reported cytoplasmic forces seven-fold larger than the aster force determined for aster-based pronuclear centering in sea urchins[7].

Combined with the rapid relaxation of devices after bending, this suggested a rapid and active softening of the cytoplasm, consistent with a shift in ξ_k corresponding to a rapid transition in stiffness from EL to DIV phases and as suggested by device behavior (Fig. 2f, left). The marked change in stiffness implied accompanying cytoskeletal rearrangement, and

α-tubulin staining revealed that embryos became depleted of microtubules over a short period as the DIV-phase reached its conclusion (Fig. 5c,d). In accordance with the small inertial forces of the embryo cytoplasm[8], nanodevices relaxed and became stationary as the division forces vanished (Fig. 5e,f and Supplementary Movie 8). Cytoplasmic stiffening during EL and rapid softening during embryo scission were reported by the nanodevices (Fig. 2f, left) and occurred in parallel with a respective increment and reduction of cytoplasmic myosin II (Fig. 5g).

Supplementary Methods

Numerical elastic simulations. The mechanical elastic performances of nanodevices and of embryos was simulated by FEM using ANSYS® Multiphysics (Release 16.0, http://www.ansys.com) as described below.

(1) Calculation of the mechanical sensitivity of the devices. The small dimensions of the devices (whose cantilever components measure 10 x 1.5 x 0.025 μm), their non-simple modal shapes, their small force constant (~10^{-3} N/m) and the fact that they are intended to be free-floating inside the cell, collectively dissuaded us from employing static or dynamic deflection techniques to derive their mechanical sensitivity, but rather argued for a dimensional calculation[1]. The nanodevices were fabricated using polysilicon deposition and patterning technologies that are highly refined in microelectronics processing, allowing a high degree of reproducibility. We empirically determined the errors in fabrication by directly measuring them (Supplementary Fig. 2) and found that variation accounted for <1.7% of errors in the values calculated for device mechanical sensitivity. However, the nanometric dimensions of the thickness of the polysilicon layer (28.7 nm) induced an uncertainty in the Young's modulus of the polysilicon layer. It is reported that silicon or polysilicon layers of less than ~100 nm thickness possess an altered Young's modulus. In one such report[9], there was a reduction from ~170 GPa (when the layers were >100 nm thick) to 68 GPa (38.5 nm) and 53 GPa (12 nm) for monocrystalline silicon layers. In the case of polycrystalline silicon (polysilicon), deposition parameters can also play a role, as they define the grain diameter. We therefore experimentally determined the Young's modulus of the polysilicon layers used by us in nanodevice fabrication using PeakForce Quantitative Nanomechanical Analysis (QNM-Brukker)[10] (Supplementary Fig. 7 and 8). This technique allows the determination of nanoscale mechanical properties by AFM nanoindentation. To this end, we used portions of

the same wafer from which the H-comb devices had been fabricated. Experiments were performed using an AFM Microscope Multimode 8 with electronic Nanoscope V (Bruker), Peak Force QNM Mode, and using a Tap525A model tip. Ten different zones across the surface of the wafer were scanned, with each scanned zone corresponding to a 5 x 5 μm^2 area comprising 512 x 512 pixels (262144 force curves). The software, Nanoscope Analysis (Bruker), extracted the Young's modulus from each force curve and calculated the percentage of the pixels with the same measured Young's modulus. The maximum of each of the plots, which approximated to a Gaussian shape, represented the Young's modulus of the polysilicon layer of the sample. We determined the Young's modulus of ten different samples in this way and averaged them. The experimental results revealed a Young's modulus of 54.4 ± 2.2 GPa for the nanodevice polysilicon layer, a value that is in good agreement with values obtained for monocrystalline silicon of similar thickness[9], corroborating our approach and the value we obtained. We accordingly adopted our experimental value for Young's modulus in the determination of nanodevice mechanical rigidity. This gave mechanical sensitivities of the nanodevices for the two proposed load conditions (Fig. 1e,f) of 0.029±0.001 μm/Pa and 0.30±0.01 μm/nN respectively. Relative errors were calculated from the analytical formulas for cantilever deflection, which are a good approximation for the two proposed symmetric load states.

Nanodevice quantitative modeling (Fig. 1e,f) was performed using the 3D element, SOLID95. The nanodevices are large enough (22.0 x 10.5 μm) compared to the embryo diameter (≥70 μm) that they can average random molecular perturbations and hence monitor cytoplasmic rearrangements. This basic assumption was validated because the nanodevices distinguished between different embryo phases, reflected by their respective distinctive force level profiles, nanodevice rotations, and changes in cytoplasmic resistance to reorganization

and mechanical activity (Fig. 2c,e,f). Moreover, the four lateral cantilevers typically exhibited similar deformations, evidencing their tendency not to respond to local (nanoscale) mechanical perturbations (for example, those produced by individual F-actin filaments or microtubules, which, at 6 nm and ~24 nm respectively, are of similar magnitudes to the nanodevice thickness: 25 nm). The nanodevices accordingly report top-down mechanical properties of the cytoplasm and are distinct from bottom-up experiments (*e.g.* based on magnetic or optical tweezers) that report local cell mechanics on the nanoscale. However, the two approaches are essential and complementary to study the different hierarchical mechanical levels inside cells. The cell interior has reduced inertial forces[8] and given this, although it is impracticable to determine the exact load conditions applied to free intracellular nanodevices, as a first approximation we modeled bending based on two representative simulations: a uniform pressure, P, applied to the device surface, or a force, F, applied at the center of the device (Fig. 1e). Given that the devices are not anchored to actin filaments or microtubules, their ends are free to rotate and translate. However, constraints in the bending direction (the perpendicular plane) acting at the ends of the comb cantilevers are required to cause nanodevice bending. Note that to achieve a given deflection by acting nearer to the nanodevice center, the force responsible would need to be larger; our force estimates therefore represent the low limit of the possible range of intracellular forces. Again, the identification of different embryo phases by their characteristic force profiles, nanodevice rotations, effective stiffness and mechanical activity corroborates this proposition (Fig. 2c,e,f).

Nanodevices exhibited initial curvatures (intrinsic deflection) of 1.3±0.3 μm due to intrinsic stress gradients that can originate during the manufacturing process or manipulation. This initial curvature induces an offset in the deflection of the nanodevices. To avoid uncertainty due to any potential initial offset, we confined our calculations to considering

variations of deflection (Fig. 2a,d,i, Fig. 5e and Fig. 6f). Furthermore, the effect of the initial curvature on the sensitivity of the devices was negligible (Supplementary Fig. 9). Stress gradients can be modelled by applying a surface stress to one side (top or bottom) of the devices. Any imbalance of surface stresses between the top and bottom induces a vertical displacement (δ_{ini}) that is perpendicular to the plane of the device. Initial curvature studies of intrinsic stresses were simulated by ANSYS using the SOLID186 element. This is a 3D 20-Node Structural Solid element that allows modeling of layered structural solids (KEYOPT(3) =1). A dummy layer with a thickness of 1/100 of the total thickness of the device was defined to simulate the surface stress effects (Supplementary Fig. 9). The second layer therefore has a thickness of 99/100 of the total thickness of the device. The two layers possess the Young's modulus for polysilicon, but an initial surface stress is applied to the dummy layer by using the INISTATE command in ANSYS to define initial states of structures. The applied surface stress in the dummy layer induces a stress gradient in the structure whose consequence is an initial offset in the displacement (δ_{ini}). Subsequently, the load steps under evaluation (pressure or force load states) are applied and simulated. These analyses (Supplementary Fig. 9) show that the initial curvature induces offsets without altering the mechanical sensitivity.

(2) GES elastic model simulation. Elastic simulations related to embryo modelling are necessarily qualitative, since the precise mechanical properties and even dimensions of the mechanical constituents are not precisely known. The finite element method (FEM) solves the equation $|F| = [K]\ |u|$, where $|F|$ is the vector of nodal forces, $|u|$ is the vector of nodal displacements (containing information about final shape deformation), and [K] is the stiffness matrix (a function of geometry and mechanical properties). Since shape deformation, $|u|$, depends on the ratio $|F|/[K]$, precise values accorded to uniform mechanical properties do not impact the deformed shape qualitatively. Notwithstanding these

basic conditions, our simulations are based on the most plausible geometric and mechanical properties of the relevant constituents. For example, models that include embryo geometry assumed that the embryo internal diameter was 70 μm and the thickness of the membrane and cortex system, 1-4 μm. For the mechanical properties of the embryo we adopted a Young's modulus of ~7,200 Pa[11]. The effective stiffness inside the embryo was simulated assuming a small force perturbation (Fig. 3f,j and Supplementary Fig. 15d-g). Since this is a static simulation, time is not relevant, but in reality, elastic deformations occur on short time scales (~1 sec). The embryo interior was modeled using the 3D element, SOLID95, and the cap (embryo cortex and membrane) with the 2D element, SHELL281. Although arbitrary mechanical properties can be employed in this model, the relationship between them is important, as it simulates a stiff external shell. Mechanical properties of the solid shell (the membrane plus cortical ensemble) and pronuclei are ~1,000-fold larger than those of the cytoplasm. This pertains except where the effect of the ratio between the Young's modulus of the shell and the cytoplasm is under investigation (Supplementary Fig. 15e).

For the GES model that assumes that the elastic contribution is greater in the direction of the displacement, we simulated only the part between the inner sphere and the cortex in the direction of the displacement. This assumption is based on the fact that the rear (the face that is opposite to the direction of the travel) part of the internal object is not attached to the sphere from which the forces is exerted.

Numerical viscous simulations

It is well known that the drag force on a sphere in a viscous fluid at very low Reynolds number is given by the Stoke's equation:

$$F = 6\pi\mu RU \qquad \text{(Equation 1)}$$

where μ is the viscosity of the fluid, R is the radius of the sphere and U is the relative velocity.

However, this law is modified in the presence of a wall, increasing the apparent viscosity of the fluid. We define a viscosity factor as the rate between effective viscosity and the molecular viscosity:

$$k_\mu = \frac{\mu_{ef}}{\mu} \qquad \text{(Equation 2)}$$

A first theoretical expression for k_μ is

$$k_\mu = \frac{1}{(1-\kappa)^2\epsilon} + \frac{1-7\kappa+\kappa^2}{5(1-\kappa)^2}\ln\frac{1}{\epsilon} \qquad \text{(Equation 3)}$$

where $\epsilon = H/R$ is the distance of the sphere to the wall, normalized with the radius of the sphere, and $\kappa = R/R'$ (<1) is the curvature of the wall with a radius R'[12,13]. Importantly, this expression is only valid for very small values of ϵ. If the sphere is inside another bigger sphere, of radius R', located at a distance x from the centre, then there are two normalized distances, $\epsilon_1 = 1/\kappa\,(1-x/R')-1$ for the contribution of the nearest wall and $\epsilon_2 = 1/\kappa\,(1+x/R')-1$ for the contribution of the farther wall. The second of these components will make only a small contribution except for spheres of relatively large radius (that is, large values of κ). The overall theoretical value of k_μ is, therefore:

$$k_\mu = k_{\mu 1} + k_{\mu 2} \qquad \text{(Equation 4)}$$

where $k_{\mu i}$ for i=1,2 is calculated with expression (3) and the respective values of ϵ_1 and ϵ_2.

To investigate the effects of the wall and the relative motion of the sphere, several simulations were performed using the open source toolbox, OpenFoam[14]. Transient simulations were performed with particles of a range of radii inside a cell of radius, 70 μm, and placed at several distances from centre of cell. Both 'outwards' (*i.e.* towards the cell wall) and 'inwards' (i.e. towards the cell centre) velocities were simulated and cell movement treated with a dynamic (deforming) computational mesh. Forces acting on the spheres were numerically computed and by the comparison with Stoke's law, the value of k_μ numerically obtained.

Supplementary References

1. Ben Ohler, “Practical Advice on the Determination of Cantilever Spring Constants”, Veeco instruments Inc. (2007).

2. Suzuki, T., et al. Mice produced by mitotic reprogramming of sperm injected into haploid parthenogenotes. *Nature Commun*. 7, 12676 (2016).

3. Chaigne, A., et al. F-actin mechanics control spindle centring in the mouse zygote. *Nat. Commun*. 7, 10253 (2016).

4. Schäfer, A, Influence of myosin II activity on stiffness of fibroblast cells, *Acta Biomater.* 1(3),273-80, (2005).

5. Chugh, P. & Paluch, E. K. The actin cortex at a glance. *J. Cell Sci* 131, 14 (2018).

6. Hose, Basarab G., et al. Reversible disassembly of the actin cytoskeleton improves the survival rate and developmental competence of cryopreserved mouse oocytes. *PLoS One*, 3, 7, e2787, (2008)

7. Tanimoto, H., Sallé, J., Dodin, L. & Minc, N. Physical Forces Determining the Persistency and Centering Precision of Microtubule Asters. *Nat. Phys*. 14, 848-854 (2018).

8. Hyman, A.A., Weber, C.A. & Jülicher, F. Liquid-liquid phase separation in biology. *Ann. Rev. Cell Dev. Biol*. 30, 39-58 (2014).

9. Xinxin, L. Ultrathin single-crystalline-silicon cantilever resonators: Fabrication technology and significant specimen size effect on Young's modulus. Appl. Phys. Lett. 83, 3081-3083 (2003).

10. Quantitative Mechanical Property Mapping at the Nanoscale with the PeakForce QNM, Application note #128, Brukker.

11. Hedrih, A.N. & Ugrčić, M. Vibrational properties characterization of mouse embryo during microinjection. Theoret. Appl. Mech. 40, 189-202 (2012).

12. Cooley, M. D. A. & O'Neill, M. E. On the slow motion generated in a viscous fluid by the approach of a sphere to a plane wall or stationary sphere. Mathematika 16, 37 (1969).

13. Cox, R. G. & Brenner, H. The slow motion of a sphere through a viscous fluid towards a plane surface—II Small gap widths, including inertial effects. Chemical Engineering Science 22, 1753-1777 (1967).

14. OpenFOAM® Documentation. (2019). Retrieved from www.openfoam.org